Daniel Anchuela Cantarero

Design and Implementation of a Spatial Biology Image-Analysis Tool for Multiplex Microscopy

MASTER'S THESIS

Supervisors: Dr. Isabel Peset Martín and Dr. Ana Cayuela López (CNIO)

Tutor: Dr. Sergio Gómez Jiménez (URV)

Master's Degree in Health Data Science

Madrid, 2025

ACKNOWLEDGMENTS

Este trabajo culmina mi Máster en Health Data Science y quiero mostrar mi gratitud a todas las personas que me han acompañado en este recorrido.

En primer lugar, gracias infinitas a mis padres y a mi hermano por apoyarme siempre, por creer en mí, sus bromas, ánimos y por esas conversaciones que me levantaban el ánimo cuando más lo necesitaba.

A Eva, por su apoyo incondicional: gracias por entender mis momentos de estrés, por animarme en cada paso y por celebrar conmigo cada pequeño avance. Tu presencia ha sido fundamental para llegar hasta aquí.

A mis amigas Bea y Andrea, con quienes compartí buena parte de los trabajos del máster: gracias por vuestra compañía, por transformar las horas de estudio en momentos divertidos y, sobre todo, por ese inolvidable Summer School.

Quiero agradecer al equipo de la Unidad de Microscopia Confocal del CNIO. A Isabel Peset, por guiarme en cada etapa del proyecto, enseñarme tanto y ofrecerme siempre comentarios constructivos; a Ana Cayuela, por su paciencia, sus consejos y su disposición constante; y a Manu, Jesús y María, por hacer de las prácticas una experiencia gratificante, compartiendo conocimientos y brindando un ambiente de trabajo excepcional. Me llevo de vosotros aprendizajes y recuerdos que valoro profundamente.

A Juan Agulló y a Héctor Peinado, del grupo Microenvironment & Metastasis, gracias por facilitarnos los datos y por confiar en mí para llevar a cabo este análisis, y a Eduardo Caleiras, por su ayuda en la anotación de las imágenes de brightfield y por compartir su experiencia como patólogo.

Al CNIO en general, gracias por brindarme la oportunidad de formarme en un entorno de excelencia. Esta etapa ha sido muy enriquecedora tanto a nivel profesional como personal, y la voy a llevar siempre conmigo.

A todos los que habéis colaborado, apoyado o animado de una u otra manera: os lo agradezco de corazón. Vuestro respaldo ha sido clave para completar este proyecto.

ABSTRACT

This work presents an integrated and validated framework for spatial tumor analysis that combines two complementary approaches. First, a modular Python pipeline is developed to process multiplex fluorescence images with an arbitrary number of channels, generated by cyclic immunofluorescence platforms. The automated workflow includes instance cell segmentation (Cellpose), cytoplasm estimation, adaptive intensity quantification, single cell phenotyping, subsequent spatial analysis, including metrics, signed distances and Voronoi diagrams, at single-cell resolution. It produces tables for fluorescence intensity quantification, binary positivity matrices, cell phenotype counts, and distance maps characterizing tumor heterogeneity, immune infiltration, and cell–cell proximity. Second, a U-Net model enhanced with Squeeze-and-Excitation attention blocks is implemented to detect invasion fronts in H&E-stained sections. Trained on over 2 000 semi-automatically annotated patches, it achieves a global F1 score of 0.82 and an AUC > 0.90. Applied to head and neck carcinomas, where this tool was rigorously validated, it revealed that approximately one-third of cytokeratin-positive epithelial cells express NGFR, with that subniche showing a 1.5× increase in proliferation (Ki-67^{+}) and enrichment for PD-L1. Furthermore, CD8^{+} T cells infiltrate the stroma more readily than macrophages, while regulatory T cells preferentially localize to NGFR^{+} regions, suggesting a localized immunosuppressive microenvironment. Containerized and compliant with OME-TIFF and CLIA standards, this pipeline offers a scalable platform for discovering and validating simultaneously multiple biomarkers in translational research and diagnostics.

RESUMEN

Este trabajo presenta un marco integrado y validado para el análisis espacial de tumores que combina dos enfoques complementarios. En primer lugar, se ha desarrollado un pipeline modular en Python para procesar imágenes de fluorescencia multiplex con un número arbitrario de canales, generadas por plataformas de tinciones de inmunofluorescencia cíclicas. El flujo automatizado incluye segmentación celular (Cellpose), estimación del citoplasma, cuantificación adaptativa de intensidad, clasificación de poblaciones celulares (subpoblaciones) y métricas espaciales, como distancias firmadas y diagramas de Voronoi, a resolución unicelular. El pipeline genera además tablas de intensidades, matrices binarias de positividad, recuentos de subpoblaciones y mapas de distancia que caracterizan la heterogeneidad tumoral, la infiltración inmune y la proximidad célula a célula. En segundo lugar, se ha desarrollado un flujo de trabajo para la detección automatizada de frentes de invasión tumorales para poder estudiar el contexto celular específicamente en estas zonas del tumor. Se ha implementado un modelo U-Net con bloques de atención Squeeze-and-Excitation para detectar los frentes invasivos en biopsias tumorales teñidas con Hematoxilina y Eosina (H&E). Entrenado con más de 2 000 parches anotados de forma semiautomática, alcanza un F1 global de 0,82 y un área bajo la curva superior a 0,90. Aplicando estos flujos de trabajo al estudio de carcinomas de cabeza y cuello, donde fue validado exhaustivamente, reveló que aproximadamente un tercio de las células epiteliales positivas para citokeratina expresan NGFR, y que ese subnicho presenta un incremento de 1,5× en proliferación (Ki-67^{+}) y un enriquecimiento en PD-L1. Además, los linfocitos CD8^{+} infiltran el estroma con mayor facilidad que los macrófagos, mientras que las células T reguladoras se localizan preferentemente en regiones NGFR^{+}, lo que sugiere un microambiente inmunosupresor localizado. Contenerizado y compatible con los estándares OME-TIFF y CLIA, este pipeline ofrece una plataforma escalable para el descubrimiento y la validación de biomarcadores espaciales en investigación traslacional y diagnóstico.

INDEX

1 INTRODUCTION 1

2 THEORETICAL FRAMEWORK AND MATERIALS 4

2.1 Spatial Tumor Biology 4
2.2 Histological Imaging and Brightfield Microscopy 5
2.3 Fundamentals of Multiplex Fluorescence Microscopy 8
2.4 Cyclic-Staining Spatial Proteomics: MACSima™ in the Technology Landscape 10
2.5 Image Analysis Foundations 12

3 METHODS 15

3.1 Tool Architecture and Rationale 15
3.2 Experimental Design and Image Acquisition 16
3.3 Instance Segmentation of Cells 22
3.4 Marker Intensity Extraction per Cell 25
3.5 Adaptive-Thresholding for Tumor Masks and cell marker Positivity 27
3.6 Cell Phenotype Definition and Counting 31
3.7 Visualization and Quality Control 33
3.8 Cell population-to-Mask Distance Measurement 36
3.9 Population-to-Population Distance Measurement 40
3.10 Automated Detection of Tumor Invasion Fronts 44

4 RESULTS 59

4.1 Deliverables of the Multiplex-Imaging Pipeline 59
4.2 Real-World Tumor-Imaging Experiment Results 59

5 DISCUSSION 72

5.1 Performance and Robustness of the Multiplex-IF Pipeline 72
5.2 Biological Insights: Tumor Heterogeneity and Immune Infiltration 73
5.3 Automated H&E-Based Detection of Tumor Invasion Fronts 73
5.4 Comparison to Existing Tools and Pipelines 74
5.5 Integration and Translational Potential 75
5.6 Ethical, Social Impact, Sustainability, and Diversity Considerations 76
5.7 Limitations and Future Directions 77

6 CONCLUSIONS 79

7 REFERENCES 82

FIGURE INDEX

Figure 1. Example multiplex image of a HNSCC ROI acquired on the MACSima™ platform. 19

Figure 2. Data structure for multi-channel fluorescence images. 21

Figure 3. Cytoplasmic estimation by morphological expansion of 3px around DAPI-segmented nuclei. 23

Figure 4. Cytoplasmic expansion enables cell-specific biomarker mapping. 24

Figure 5. Pseudo-colored labeled mask: each segmented cell is uniquely colored (IDs 1–n) and background pixels (ID 0) are black. 25

Figure 6. Mean fluorescence-marker intensity extraction for a given Cell. 26

Figure 7. (A) Clean nuclear Ki67 staining (magenta) with no background. (B) FoxP3 staining (red) showing diffuse background; only the brightest spots correspond to true positives. 28

Figure 8. Example workflow for CK-based tumor mask generation. 29

Figure 9. Multi-panel visualization of imaging, segmentation and CK^+ /$CD3^+$ subpopulation selection. 36

Figure 10. Schematic of the sub-population-to-mask distance measurement. 39

Figure 11. Conceptual schematic of subpopulation-to-subpopulation distance measurement. 41

Figure 12. Voronoi tessellation of Subpopulation 1 (blue crosses) showing how each polygonal region (green edges) defines the nearest-neighbor territory around each reference cell. 42

Figure 13. Representative whole-slide H&E image of an HNSCC biopsy. 45

Figure 14. Semi-automatic annotation workflow: (A) manual invasion-front polygons, (B) inverted non-front mask, and (C) final three-class map. 46

Figure 15. Stain-space decomposition of an H&E-stained RGB patch into separate hematoxylin (nuclear) and eosin (cytoplasmic/stromal) optical-density channels. 47

Figure 16. Histograms of tile class proportions, showing the distribution of background, invasion-front epithelium, and stroma across 2 003 patches. 48

Figure 17. Histograms of mean grayscale brightness and normalized hematoxylin and eosin intensities, illustrating the consistency of staining across all tiles. 49

Figure 18. Annotated Pearson correlation matrix between class proportions and photometric features, highlighting positive and negative inter-feature relationships. ... 50

Figure 19. Scatter plot of invasion-front proportion versus mean hematoxylin intensity, with point color indicating stromal proportion. 51

Figure 20. Scatter plot of stromal proportion versus mean eosin intensity, with point color indicating invasion-front proportion. 51

Figure 21. Scatter plot of background proportion versus mean grayscale brightness, with point color indicating invasion-front proportion. 52

Figure 22. Box-plots of mean eosin and hematoxylin intensities stratified by stromal-proportion quartiles (Q1–Q4). 52

Figure 23. Pairwise scatter matrix of six key features with diagonal kernel-density estimates, colored by each tile's dominant class. 53

Figure 24. Diagram of the U-Net architecture with Squeeze-and-Excitation and dilated convolutions. 55

Figure 25. Tumor-characterization bar plots showing the fraction of CK^+ cells that are $NGFR^+$ versus $NGFR^-$ and their Ki-67, CD274, IFN-γ and HLA-DR positivity rates for each ROI. 60

Figure 26. Tumor-infiltration bar plots showing the intratumoral versus stromal distribution of selected immune subpopulations for each ROI. 61

Figure 27. Tumor-infiltration bar plots showing the intratumoral distribution of selected immune subpopulations for each ROI stratified by NGFR positivity. 62

Figure 28. Interactive validation panels for ROI 11 showing IFN-γ^+ cell overlays and counts: 485 IFN-γ^+ cells in CK^+ $NGFR^+$ regions (row 2) and 138 IFN-γ^+ cells in CK^+ $NGFR^-$ regions (row 3). 63

Figure 29. Overlay of Treg centroids (yellow) and signed-distance vectors to the CK mask in two regions: (A) ROI 11, showing long distance vectors consistent with a larger field and stromal exclusion; and (B) ROI 7..... 64

Figure 30. Violin-and-boxplots of signed Euclidean distances (d(CK)) for regulatory T cells across all six ROIs. 65

Figure 31. Voronoi tessellation overlays of Treg-to-epithelium distances in ROI 11, comparing proximity to CK^+ $NGFR^+$ (A) versus CK^+ $NGFR^-$ (B) epithelial cells. 66

Figure 32. Boxplots of Treg-to-epithelium distances across all six ROIs for CK^+ $NGFR^+$ (green) versus CK^+ $NGFR^-$ (orange) compartments, showing nearly identical distributions. 66

Figure 33. Scatter plot of predicted vs. true tumor-FOI pixel counts (dashed identity line). 67

Figure 34. Normalized confusion matrix showing recall rates for background, FOI, and stroma. 68

Figure 35. Intersection-over-Union and Dice scores per class. 69

Figure 36. Accuracy, precision, recall, F1-score, and accuracy for each class..... 69

Figure 37. Overall accuracy, precision, recall, and F1-score across all pixels. 70

Figure 38. ROC curves with AUC values for background, FOI, and stroma.. 70

Figure 39. Box plots of per-patch IoU for FOI and stroma. 71

Figure 40. Representative three-panel overlay: original, predicted, and ground truth. 71

TABLE INDEX

Table 1. Conceptual advantages shared by all cyclic-staining spatial-proteomics platforms. 10

Table 2. Positioning MACSima™ (MICS) among the main cyclic-staining platforms used for spatial proteomics. 11

Table 3. Channel-to-Biomarker Mapping of the 22-Marker Panel (channels used to define sub-populations shown in bold). 17

Table 4. Geometric properties, channel count and QC status of each ROI. 20

Table 5. Optimized Cellpose parameters for nuclear segmentation. 22

Table 6. Illustrative per-cell mean-intensity table showing cytokeratin (CK) status and mean fluorescence for CD3 and Ki67. 27

Table 7. ROI-specific scaling factors used for NGFR thresholding. 29

Table 8. Global scaling factors *k* for marker-specific positivity calls. 30

Table 9. Illustrative binary master table of per-cell positivity calls for CK, CD3 and Ki-67. 31

Table 10. Marker-Specific Positivity Rules for Immune Phenotypes. 32

Table 11. Tumor Characterization Subpopulations (HNSCC) 32

Table 12. Tumor Infiltration Subpopulations (HNSCC) 33

Table 13. Tumor Infiltration Related to NGFR. 33

Table 14. Training hyper-parameters and rationale. 56

1 INTRODUCTION

Cancer is not merely a disease but rather a complex and evolving ecosystem characterized by dynamic interactions among tumor cells and their surrounding microenvironment [1]. Understanding cancer as a spatially organized entity is crucial for developing effective diagnostic tools and therapies. Traditionally, the spatial organization and histological features of tumors have been studied using brightfield microscopy on tissue sections stained with Hematoxylin and Eosin (H&E) [2]. H&E staining is considered the gold standard in pathology due to its cost-effectiveness, simplicity, and ability to provide detailed morphological information [2]. However, despite its extensive clinical use, brightfield microscopy and conventional histology staining present significant limitations. Most notably, these approaches fail to capture multiple molecular-level information, limiting their ability to discern different cell types simultaneously, functional states, and specific molecular interactions.

Brightfield microscopy images typically rely on the manual interpretation of tissue morphology by experienced pathologists, introducing variability, subjectivity, and limited scalability [3]. Although crucial for diagnosis, prognosis, and treatment decisions, histopathological assessments based solely on H&E or single biomarker staining lack the depth necessary to understand complex biological processes like tumor heterogeneity, immune infiltration, and molecular gradients within the tumor microenvironment.

Recent advancements in fluorescence microscopy, particularly in multiplex imaging and spatial biology, have initiated a paradigm shift, significantly enhancing our ability to understand tumors at a cellular and molecular level. Multiplex fluorescence imaging techniques, such as amplification signal techniques, cyclic immunofluorescence, and mass-tag imaging, allow simultaneous visualization and quantification of dozens to hundreds of molecular markers within a single tissue section, preserving spatial relationships at single-cell resolution [4], [5], [6]. These techniques represent a revolutionary step beyond conventional brightfield microscopy, as they provide comprehensive "who-what-where" information—identifying cell types ("who"), their molecular profiles ("what"), and their precise locations within tissue architecture ("where"). The ability to integrate spatial, molecular, and cellular data has turned spatial

biology into a cornerstone of modern oncology research, as evidenced by Nature Methods declaring spatial proteomics the "Method of the Year 2024" [7].

Given this context, the overarching goal of this master's thesis is two-fold, aimed at integrating cutting-edge fluorescence multiplex imaging analysis with traditional histopathological approaches to enhance our understanding of tumor invasion patterns:

First, the project focuses on developing a comprehensive, modular, and scalable analytical pipeline specifically designed to analyze multiplex fluorescence microscopy images of 15-20 cellular markers. This pipeline addresses existing gaps in spatial proteomics analysis by providing robust computational tools for automated single cell segmentation, adaptive marker quantification, cell phenotyping, and sophisticated spatial metrics, thus enabling the detailed exploration of spatial heterogeneity, cellular interactions, and microenvironmental dynamics.

Secondly, recognizing the clinical and biological importance of tumor invasion fronts, the thesis addresses the critical need to identify and characterize these specific regions within traditional histological brightfield images stained with H&E. Tumor invasion fronts are regions where active tumor progression and interaction with the stroma occur, often associated with aggressive cancer phenotypes, therapy resistance, and poor prognosis [8]. Therefore, accurately detecting and analyzing these regions is essential for targeted biological analyses. To achieve this, the thesis incorporates advanced computational methodologies, including deep learning and specifically a U-Net convolutional neural network architecture [9], to automatically detect invasion fronts in brightfield histological images.

The development of this automated deep-learning-based tool is justified by recent advances in computational capabilities, specifically the accessibility of high-performance GPUs, which have enabled more efficient training and deployment of sophisticated deep learning models [10]. By harnessing these computational advances, the proposed model aims to generalize across diverse histological samples, reliably identifying invasion fronts without extensive manual annotations.

Overall, the integration of these two innovative analytical approaches is strategically designed to focus multiplex fluorescence analysis specifically on biologically critical regions identified by the deep-learning-based invasion front detection. Instead of analyzing entire tissue sections, which may dilute biologically meaningful insights, this combined strategy ensures the multiplex imaging analysis targets regions of greatest clinical and biological significance.

Ultimately, this thesis presents a unified framework that leverages both high-dimensional fluorescence imaging and advanced histopathology to interrogate tumor invasion. First, a flexible, Python-based pipeline is established for processing cyclic immunofluorescence data from 15–20 markers, enabling automated single-cell segmentation, adaptive intensity quantification, and phenotypic classification to map cellular heterogeneity and microenvironmental interactions at single-cell resolution. Concurrently, a deep-learning module based on a U-Net architecture is developed to identify invasion fronts within standard H&E-stained sections, providing precise tumor-stroma boundaries without extensive manual annotation. By coupling these two approaches, the multiplex fluorescence analysis is directed exclusively to biologically relevant invasion regions—rather than the entire tissue—thereby maximizing the likelihood of uncovering clinically significant patterns of cellular organization, immune infiltration, and proliferative niches at the tumor's leading edge.

2 THEORETICAL FRAMEWORK AND MATERIALS

2.1 Spatial Tumor Biology

Spatial biology quantifies molecular events in situ, retaining the exact x- and y-coordinates of every measurement in a tissue section. In contrast, bulk assays—flow cytometry, RNA-seq, mass-spectrometry proteomics—obliterate architecture by pooling thousands of cells. Spatial approaches therefore integrate who, what, and where: single-cell identity ("who"), molecular phenotype ("what") and physical position ("where"). By coupling these three axes, spatial biology unveils emergent properties such as cell–cell cooperation, niche formation and gradient sensing—phenomena that disappear once tissue is homogenized. The discipline has expanded explosively over the last five years, fueled by advances in high-content imaging and by spatial omics starting to become routine in both academia and biotech [6], [11], [12], [13].

2.1.1 Relevance in Oncology

Cancer is an intrinsically spatial disease. Clonal evolution creates genetic and phenotypic mosaics within the same tumor; immune surveillance sculpts patchy "hot" and "cold" regions; and stroma, vasculature and nerves generate micro-ecosystems with distinct pH, oxygen tension and cytokine milieus. Whereas bulk measurements average these gradients away, spatial read-outs:

- Map clonal heterogeneity, revealing whether therapy resistant subclones are clustered or dispersed.
- Trace immune landscapes, distinguishing infiltrated nests from immune excluded cores.
- Identify functional niches such as hypoxic rims or NGFR-rich epithelial pockets that may fuel invasion or drug resistance.

These insights translate directly into prognostic biomarkers and rational combination therapies—one reason *Nature Methods* named spatial proteomics "Method of the Year 2024" [7].

2.1.2 Historical Perspective

Spatial biology began with single-marker immunofluorescence in the 1950s and expanded in the 1990s when multispectral microscopy enabled several markers in parallel. During the 2010s, iterative staining strategies and metal-based imaging pushed multiplexing further, while advances in automation and machine learning lowered the barrier to routine adoption. Today, laboratories can routinely profile hundreds of proteins at sub-cellular resolution [14][15][16], shifting spatial analysis from niche experimentation to high-throughput discovery.

2.1.3 Emerging Clinical Applications

Spatial read-outs are already woven into pathology—single-marker assays such as PD-L1 IHC or HER2/neu ISH guide treatment decisions worldwide. Multi-marker spatial proteomics is now appearing in late-phase clinical trials [12] to quantify immune exclusion, stratify responders to checkpoint blockade and profile tumor–immune niches relevant to cell-therapy efficacy. Regulatory review of high-plex panels is under way, signaling that spatial biomarkers are on the cusp of routine clinical deployment.

2.2 Histological Imaging and Brightfield Microscopy

Brightfield review of Hematoxylin-and-Eosin (H&E) sections is still the first—and often the only—microscopic examination performed on every surgical specimen. It anchors the diagnostic workflow, guides ancillary testing, and supplies the morphological context into which all high-dimensional (read “omics”) measurements must ultimately be mapped. The following sections summarize the chemical principles, optical foundations, and practical limitations of this century-old technique so that its strengths—and its blind spots—are explicit before we move on to multiplex fluorescence and spatial analytics.

2.2.1 Fundamentals of H&E Staining

Hematoxylin-and-eosin delivers a high-contrast, stable record of tissue architecture in fewer than ten minutes and at negligible reagent cost.

- **Chemical basis.** Hematoxylin, oxidized to hematein and complexed with aluminum or iron mordant, behaves as a basic (cationic) dye and binds strongly to anionic phosphate backbones in DNA and RNA, staining nuclei blue-purple. Eosin Y is weakly acidic; it electrostatically labels protonated amino groups on cytoplasmic and stromal proteins, imparting a pink–orange hue.

- **Routine workflow.** After deparaffinization and hydration, slides pass through hematoxylin, bluing solution, eosin, graded alcohols, xylene, and coverslip. Precise timing of differentiation and bluing is critical for crisp nuclear detail.

- **Diagnostic information.** The complementary stains separate basophilic nuclei from eosinophilic cytoplasm and extracellular matrix, revealing cell density, gland formation, necrosis, hemorrhage, and stromal reaction briefly.

- **Quality variables.** Fixation time, dye oxidation state, water purity, and section thickness all modulate final chromatic balance; automated stainers reduce—yet never abolish—batch-to-batch variability.

2.2.2 Principles and Scope of Brightfield Microscopy

Brightfield is the simplest transmission modality and the default for H&E review.

- **Optical path:** White light, shaped by field and condenser diaphragms under Köhler illumination, traverses the stained section. Differential absorption and scatter encode contrast; the objective collects and magnifies the emergent wavefront for eyepiece or camera.

- **Resolution and magnification:** Properly aligned optics deliver diffraction-limited performance (≈0.25 µm with a 40×, NA 0.95 objective). Pathologists survey at 4×, interpret at 10–20×, and confirm cytology at 40–60×; digital scanners mimic this pyramid, storing base layers at 0.22–0.50 µm px^{-1}.

- **Digital extensions:** Whole-slide imaging feeds morphometry, color deconvolution, and machine-learning pipelines (HALO, QuPath, Visiopharm) that convert qualitative impressions into semi-quantitative features.

- **Clinical reach:** Brightfield H&E underpins grading, staging, and margin status for virtually every solid tumor and remains the triage gatekeeper for immunohistochemistry (IHC), in situ hybridization, and next-generation sequencing.

2.2.3 Limitations: Why Morphology Alone Is Insufficient

Even a perfectly executed H&E slide provides, at best, a morphological snapshot. That snapshot is indispensable—but it is also incomplete. The key limitations are:

- **Invisible functional diversity.** Exhausted versus cytotoxic T cells, M1- versus M2-polarized macrophages, and genetically divergent tumor sub-clones all look essentially identical in hematoxylin-and-eosin. With no molecular layer, H&E cannot reveal which cells drive immune escape, harbor resistance mutations, or secrete pro-metastatic cytokines.

- **Observer dependence and limited reproducibility.** Architectural patterns such as "tumor budding" or "lymphovascular invasion" hinge on manual interpretation. Inter-observer κ values for common grading tasks frequently fall in the 0.4–0.6 range, reflecting genuine subjectivity that no amount of optical finesse can eliminate.

- **Multiplex ceiling.** Chromogenic immunohistochemistry marginally extends brightfield to two or three markers, but stain overlap, spectral crowding, and iterative destain/re-stain cycles impose a hard stop well below the dimensionality required to profile modern oncologic pathways.

- **Sampling bias and two-dimensionality.** A 4-µm section represents a fraction of a percent of the tumor volume and collapses the z-axis, obscuring 3-D gradients of hypoxia, pH, and immune infiltration that unfold over tens to hundreds of microns.

- **Static endpoint.** Fixation freezes tissue in time; dynamic processes—checkpoint engagement, signaling cascades, cytokine bursts—remain invisible.

These blind spots create a diagnostic and research "information gap" that demands complementary technologies capable of multiplex, quantitative, and spatially resolved molecular read-outs.

2.3 Fundamentals of Multiplex Fluorescence Microscopy

Multiplex fluorescence microscopy (MFM) extends conventional histology by turning a two-color H&E section into a high-dimensional molecular map. Instead of examining one or two chromogenic stains, investigators can visualize dozens of molecular targets in the very same tissue plane, linking morphology with rich phenotypic detail at single-cell resolution.

2.3.1 Why Multiplex vs. Brightfield?

MFM overcomes three longstanding limitations of brightfield imaging:

- **Depth of information** – Many proteins or nucleic-acid features can be detected simultaneously, revealing cell states and signaling pathways that look identical in H&E.
- **Spatial precision** – Every fluorescent tag is registered to an individual cell, preserving neighborhood relationships that disappear in bulk assays or serial IHC.
- **Quantitative linearity** – Fluorescence intensity scales linearly across a wide dynamic range, enabling per-cell comparisons within and across specimens.

Together, these advantages fill the "morphology gap," supplying objective, multiplex data while maintaining the architectural context pathologists rely on.

2.3.2 Photophysical Principles and Channel Management

Fluorophores absorb light at an excitation wavelength and emit at a longer wavelength (the Stokes shift). Key considerations for fluorophore selection include emission peak separation, brightness, photostability and compatibility with tissue autofluorescence.

Successful multiplexing hinges on careful allocation of those emission bands so that signals remain optically distinguishable. Three strategies work in concert:

1. **Spectral separation** – Choose dyes with well-spaced emission peaks and match them to narrowband filters to minimize crosstalk.

2. **Spectral unmixing** – When minor overlaps are unavoidable, reference spectra can be used to computationally disentangle signals after acquisition.

3. **Balanced exposure** – Dye concentrations and exposure times are adjusted so dim channels stay above detector noise while bright channels avoid saturation, preserving quantitative integrity.

In practice, each fluorophore is also evaluated for photostability—ensuring it resists photobleaching over multiple imaging cycles—and for minimal background in fixed tissue. By pairing robust antibodies with an optimized fluorophore panel, one maintains both signal fidelity and multiplex depth.

Before imaging, one must assemble an antibody panel that covers every biological compartment of interest—tumor epithelium, immune lineages, functional states (e.g., proliferation, checkpoint markers), and stromal or vascular elements—while minimizing spectral overlap. This involves selecting one well-validated antibody clone per compartment and assigning each to a fluorophore whose emission band does not conflict with others. By conceptually matching each antigen to a distinct channel and balancing relative fluorophore brightness, the panel maximizes detectability of low abundance targets and prevents crosstalk [14].

2.3.3 Cyclic Multiplexing Workflow

Because the visible spectrum supports only a handful of non-overlapping fluorophores at once, modern workflows adopt an iterative stain–image–remove cycle. A subset of markers is applied, imaged, chemically or photochemically cleared, and the process repeats until all targets are recorded. Fiducial landmarks—such as a nuclear counterstain—provide a constant reference so that images from successive cycles can be

precisely aligned, assembling a comprehensive stack that still reflects the original tissue architecture.

2.3.4 Key Technical Challenges

High-plex imaging introduces technical challenges—including photobleaching, tissue autofluorescence, mechanical drift between cycles, and incomplete reagent stripping—that can propagate through segmentation and downstream analytics. Dedicated quality-control checkpoints and appropriate correction algorithms are therefore integral parts of any robust MFM workflow.

2.4 Cyclic-Staining Spatial Proteomics: MACSima™ in the Technology Landscape

Cyclic-staining methods form the proteomic branch of spatial biology: a single tissue section is iteratively stained, imaged, and chemically or photochemically reset, allowing tens-to-hundreds of antibody targets to be recorded in the exact same cellular coordinates. As Table 1 highlights, all platforms that follow this "cycle–image–elute" paradigm share four conceptual advantages over one-shot multiplex kits or bright-field IHC.

Table 1. Conceptual advantages shared by all cyclic-staining spatial-proteomics platforms.

Core advantage	Rationale
Unlimited plex (linear-with-cycles)	A fixed 4–7-channel microscope can capture 40, 60, or 100+ epitopes simply by adding cycles.
Single-section integrity	Every target is measured on the same slice, eliminating registration drift between serial sections.
Quantitative fluorescence read-out	Linear 16-bit signal enables per-cell intensity statistics and cross-sample normalization.
Architecture preserved	Neighborhoods, gradients, and rare niches remain intact—none of the spatial cues are lost to tissue pooling.

2.4.1 Representative Implementations

Commercial and academic solutions differ in detection chemistry, degree of automation and the trade-off between speed, cost and resolution. Table 2 provides a qualitative overview of the four families most cited in the literature.

Table 2. Positioning MACSima™ (MICS) among the main cyclic-staining platforms used for spatial proteomics.

Platform	Detection modality	Typical plex	Lateral resolution	Key strength	Key limitation
IMC (Imaging Mass Cytometry) [15]	Metal-tag antibodies, laser ablation + TOF-MS	40–50	1 µm	Zero optical background; high antibody plex	Ablative; > 2 h per cm² acquisition
CODEX [4]	DNA-bar-coded antibodies + cyclic fluorescent read-out	40–60	0.5 µm	Commercial kits; open antibody ecosystem	Semi-manual fluidics for large panels
CyCIF [16]	Iterative stain–image–bleach fluorescence	60–80	0.3 µm	Uses standard scanners; flexible dyes	Photobleaching efficiency is critical
MACSima (MICS) [17]	Fully automated cyclic immunofluorescence in closed cartridge	100 +	0.2 µm	Hands-off workflow; high cycle reproducibility	Capital cost; proprietary reagents

2.4.2 Distinctive Features of Fully Automated Platforms

Systems such as MACSima™ MICS carry the stain–image–elute concept to its logical extreme—every fluidic, optical and data-handling step is scripted from start to finish. Their hallmark traits are:

- **End-to-end automation**: Closed cartridges with programmable fluidics and stable environmental control minimize operator variability.

- **High plex without custom chemistry**: Ready-to-use, pre-conjugated antibodies remove in-house labelling steps and simplify inter-laboratory standardization.
- **Routine-friendly cadence**: Panels of several dozen markers can be completed overnight, dovetailing with the daily workflow of diagnostic histopathology.
- **Data interoperability**: Export to open image and metadata formats enables inspection in free viewers and reproducible analysis in Python/R.
- **Regulatory traction**: Clinically certified reagents accelerate the translation of spatial proteomics from research into routine practice.

These attributes place fully automated cyclic-staining systems in the "high-plex / high-reproducibility" corner of the technology spectrum, complementing alternatives such as IMC, CODEX and CyCIF according to the resolution, throughput and cost constraints of each study.

2.5 Image Analysis Foundations

Modern spatial-omics studies convert a multichannel fluorescence stack into quantitative, per-cell data. Three fundamental blocks underpin that conversion:

1. **Tissue-compartment masking**: Delineating broad anatomical regions (e.g., tumor vs. stroma) so that every cell can be assigned to a spatial context.

2. **Cell segmentation**: Identifying the pixels that belong to each individual cell.

3. **Deep-learning segmentation**: Advanced convolutional-encoder/decoder models that refine the cell-segmentation step by predicting per-pixel flows or boundaries.

2.5.1 Tissue-Compartment Masking

To pose spatial questions—such as how far an immune cell has infiltrated into a tumor region—one first needs a binary map of the compartment of interest. In epithelial tumors, a specific epithelial marker immunostaining is typically used to delineate the malignant region, while all pixels outside that area are treated as non-tumor.

Binary masks enable three key operations:

- **Compartment annotation**: assigning each segmented cell as intratumoral or stromal by testing whether its centroid lies inside the designated epithelial region.
- **Distance transforms**: converting the mask to a signed Euclidean distance field (negative inside, positive outside) that quantifies exclusion versus infiltration on a continuous scale.
- **Logical gating**: combining the presence or absence of any given marker with mask membership to define biologically meaningful subsets (for example, selecting a specific immune phenotype only within the epithelial region).

Mask quality is safeguarded by a short QC pipeline: global or locally adaptive thresholding converts fluorescence to a binary image; small debris is removed; and interior holes are filled to ensure continuity. These steps minimize false boundaries and produce masks that are ready for high-level spatial statistics.

2.5.2 Cell Segmentation

A universal nuclear dye provides a bright, high-contrast signal that anchors segmentation in nearly any tissue. Classical watershed and threshold routines remain useful, but state-of-the-art workflows increasingly rely on convolutional-neural-network models that predict per-pixel flow fields or boundary probabilities. Importantly, these learning-based methods perform instance segmentation—differentiating individual nuclei or cells by assigning a distinct mask to each object—thereby ensuring that each cell is segmented as a unique instance and avoiding overlaps. These learning-based methods generalize across diverse cell shapes and densities with minimal manual tuning.

This kind of analyses often require cytoplasmic or membrane signal as well as nuclear signal. A common solution is to expand each nuclear mask outward by a small, uniform margin, creating an approximate whole-cell outline that captures extranuclear biomarkers without substantially increasing computational load.

2.5.3 Deep-learning segmentation

State-of-the-art tissue segmentation is now dominated by convolutional encoder–decoder networks that combine three design elements: (1) a U-Net skeleton whose skip-connections preserve pixel-level detail while the bottleneck captures global context; (2) attention gates—for example, squeeze-and-excitation blocks—that re-weight feature maps according to scene context [20]; and (3) dilated convolutions that enlarge the receptive field without extra pooling [21], allowing the model to integrate information across several histological scales.

Effective training hinges on composite objectives that couple a region-overlap term (Dice / IoU) with a pixel-wise loss (cross-entropy), tuned by adaptive optimizers and tempered through learning-rate decay. Robustness is increased by aggressive data augmentation (rotations, color jitter, elastic deformations), lightweight regularization (weight-decay, dropout) and early stopping on an independent validation fold.

At inference time, raw probability maps benefit from post-processing: small-object filtering removes spurious islands, edge-preserving smoothing restores boundary continuity, and uncertainty maps (e.g. maximum soft-max) flag low-confidence regions for optional human review. Performance is summarized with pixel-level Dice/IoU, object-level precision-recall and a confusion matrix that pinpoints systematic mis-classifications—metrics that together provide a balanced view of accuracy, completeness and clinical usability.

3 METHODS

This study presents a comprehensive, modular analysis pipeline tailored for spatial biology workflows using multiplex fluorescence microscopy data, with a focus on tumor samples acquired via the MACSima™ platform. In this section, each component of the tool is described in detail while, in parallel, its application is illustrated using a real head-and-neck squamous-cell carcinoma (HNSCC) dataset obtained with MACSima™. Accordingly, the narrative alternates between (1) a generic description of each pipeline module and (2) the specific choices made for the HNSCC study, demonstrating how every step—from image loading and cell segmentation to advanced spatial analyses—is implemented and adapted to a real-world experiment.

3.1 Tool Architecture and Rationale

The primary goal was to create a flexible, general-purpose pipeline for analyzing multiplex fluorescence images. The pipeline integrates:

- Data Input: Reading large *.ome.tif* or *.tif* files containing multiple fluorescent channels.
- Segmentation: Automatic, instance-level identification of cells (nuclei or nuclei and cytoplasms).
- Marker Quantification: Measuring fluorescence intensities for each segmented cell across all channels.
- Positivity Assignment: Applying adaptive thresholds to classify each cell as positive or negative for given markers.
- Cell Phenotyping: Grouping cells according to logical marker-expression patterns (e.g., T cells, macrophages, etc.).
- Spatial Analyses: Calculating distances from cells to tumor regions (or stroma), as well as cell-to-cell distances for immune cells tumor infiltration studies.

- **Visualization**: Generating both numeric data (tables of counts, distances) and overlay images to verify or illustrate the analysis.
- **Automated Detection of Tumor Invasion Fronts**: U-Net with Squeeze-and-Excitation attention to segment invasion fronts on H&E images, including stain deconvolution and light morphological postprocessing.

The modular design ensures each step can be replaced or modified with minimal disruption. For instance, users may choose Cellpose or an alternative segmentation algorithm, or define custom thresholds and subpopulations as needed.

3.2 Experimental Design and Image Acquisition

To illustrate the application of the analytical pipeline, a head-and-neck squamous-cell carcinoma (HNSCC) study was conducted. These tissue sections were obtained through collaboration with Hector Peinado's laboratory, the Microenvironment & Metastasis Group. Tissue sections, enriched for oropharyngeal cases and including regions of premalignant epithelium, were processed on the MACSima™ cyclic-staining platform. The study had three primary aims:

1. **Characterize the spatial distribution of immune cells** relative to epithelial compartments (premalignant versus malignant) in HNSCC tumor cores.
2. **Evaluate the intrinsic phenotype of NGFR$^+$ tumor cells** by quantifying co-expression of the proliferation marker Ki-67 and immunoregulatory markers PD-L1 (CD274) and HLA-DR.
3. **Determine associations between NGFR expression and local immunosuppression** by measuring the proximity of NGFR$^+$ cells to distinct immune subsets.

To achieve these aims, a multiplexed imaging experiment generated high-dimensional fluorescence data from multiple regions of interest (ROIs) per sample. Below, the imaging strategy and sample selection are described first, followed by details on the marker panel and ROI quality control, and finally the organization and ingestion of raw image files into the computational pipeline.

3.2.1 Imaging Strategy and Marker Panel

Multiplex imaging was performed on the MACSima™ cyclic-staining platform by selecting Regions of Interest (ROI) from a low resolution DAPI image in each tumor biopsy. Using a 20× objective NA 0.45 (0.17µm/px, 16-bit depth), twenty-two fluorescence channels. The marker panel encompassed four functional classes:

- **Tumor / Epithelial Markers**: Pan-Cytokeratin (CK) and NGFR, used to delineate epithelial compartments and to distinguish $NGFR^{+}$ from $NGFR^{-}$ tumor cells.

- **Immune Markers**: Lineage markers (CD3, CD4, CD8α, CD20, CD56), myeloid markers (CD68, CD11b, CD11c, CD163), and pan-leukocyte marker CD45, enabling identification of T cells, B cells, macrophages, dendritic cells, and other leukocyte subtypes.

- **Functional-State Markers**: Ki-67 (proliferation), PD-1 and PD-L1 (immune checkpoints), IFN γ (cytokine release), and HLA-DR (antigen-presenting activity), facilitating phenotypic characterization of activation status and checkpoint expression.

- **Structural Markers**: CD31 (endothelial), α-Actin (stromal), and Podoplanin (lymph-node–associated stroma), providing context on vasculature and stromal architecture.

All twenty-two channels remain available throughout data processing. However, only fourteen of these markers—those essential for defining the cell populations of interest—are used in binary classification logic. The full channel-to-biomarker mapping is shown in Table 3, with channels used for subpopulation definitions indicated in **bold**.

Table 3. Channel-to-Biomarker Mapping of the 22-Marker Panel (channels used to define sub-populations shown in bold).

Channel #	Biomarker	Channel #	Biomarker
0	**FOXP3**	11	α-Actin
1	**IFN-γ**	12	CD31
2	CD20	**13**	**NGFR**
3	**HLA-DR**	**14**	**DAPI**
4	PD-1 (CD279)	**15**	**CD3**
5	**CD4**	16	CD56
6	Podoplanin	**17**	**PD-L1 (CD274)**
7	**Ki-67**	18	CD45
8	CD163	**19**	**CD11c**
9	**CD11b**	**20**	**CD8α**
10	**Pan-Cytokeratin (CK)**	**21**	**CD68**

CK and NGFR channels are used to generate epithelial masks—one for the overall tumor compartment and one for NGFR sub-compartmentalization—while DAPI (channel 14) serves exclusively for nuclear segmentation. All subsequent steps (segmentation, intensity extraction, thresholding) refer to the same 22-channel structure, ensuring consistency across analyses.

As an illustrative example of our multiplex acquisition, Figure 1 presents a representative ROI from a HNSCC sample. In Panel A, the five selected fluorescence channels are overlaid to show the composite distribution of Pan-Cytokeratin (CK), DAPI, CD3, CD4, and FOXP3. Panel B isolates the CK channel to highlight the epithelial compartment, while Panel C shows the DAPI signal used for nuclear segmentation. Panel D displays $CD3^+$ cells, Panel E shows $CD4^+$ cells, and Panel F depicts $FOXP3^+$ cells. Together, these panels demonstrate how individual markers appear both separately and in combination within a single field of view.

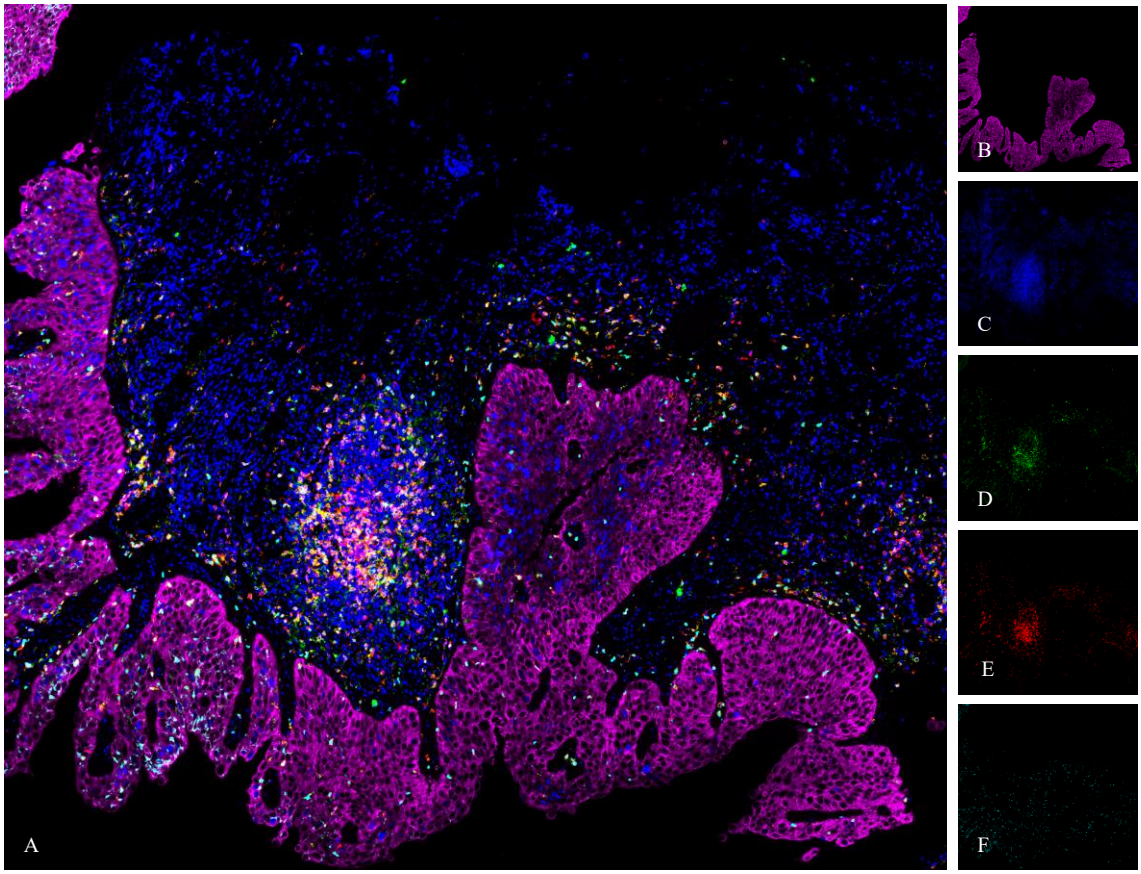

Figure 1. Example multiplex image of a HNSCC ROI acquired on the MACSima™ platform.

3.2.2 Region Of Interest Selection and Quality Control

Thirteen non-overlapping ROIs were selected to capture both premalignant epithelial patches and overt carcinoma within each tumor biopsy core. Imaging parameters (objective, exposure time and light power) were applied uniformly across all ROIs, using the full 22-marker panel plus DAPI.

Immediately post-acquisition, each ROI underwent a standardized quality-control (QC) workflow:

1. **Staining Uniformity**: A visual inspection confirmed even signal intensity across all 22 cycles, ruling out uneven antibody binding or focal signal dropout.

2. **Cycle Registration**: Successive imaging rounds were verified to be aligned with sub-pixel accuracy, ensuring that multi-cycle composite images would not suffer registration artifacts.

3. **Tissue Integrity**: Each ROI was examined for tears, folds, or localized tissue loss that could bias quantification (e.g., missing cells or distorted morphology).

Following QC, seven of the original thirteen ROIs were excluded due to irregular staining, artifacts, or tissue damage. The remaining six ROIs (ROI 5, ROI 6, ROI 7, ROI 8, ROI 11, and ROI 13) met all QC criteria and were carried forward. Geometric properties, channel count, and QC status of each ROI are summarized in Table 4.

Table 4. Geometric properties, channel count and QC status of each ROI.

ROI	Height (px)	Width (px)	Pixel size (µm / px)	Channels (n)	QC status
ROI1	7 700	9 322	0.17	22	Discarded
ROI2	7 701	9 335	0.17	22	Discarded
ROI3	7 700	9 328	0.17	22	Discarded
ROI4	7 703	9 321	0.17	22	Discarded
ROI5	7 702	9 321	0.17	22	**Included**
ROI6	7 704	9 324	0.17	22	**Included**
ROI7	7 702	9 323	0.17	22	**Included**
ROI8	10 223	9 321	0.17	22	**Included**
ROI9	7 704	9 341	0.17	22	Discarded
ROI10	7 705	9 317	0.17	22	Discarded
ROI11	7 707	9 312	0.17	22	**Included**
ROI12	7 704	9 313	0.17	22	Discarded
ROI13	7 701	9 453	0.17	22	**Included**

3.2.3 File Organization and Data Ingestion

After QC, raw image files (multi-channel TIFF or OME-TIFF) were ingested into the computational workflow. The following conventions and steps governed file organization and ingestion:

1. **File Naming and Structure:** Each ROI's image file was named according to a structured convention—e.g., ROI005.ome.tif—encoding sample identifiers and ROI numbers. This naming scheme enabled automated parsing scripts to assign each image to its metadata record, preserving the link between image data and experimental annotations (such as patient ID, tissue block, and staining batch).

2. **Loading and Stacking Channels**

- **Image Reading**: Each TIFF/OME-TIFF file was loaded into memory and converted into an array with shape (channels × height × width). For the HNSCC experiment, each array comprised 22 slices (21 marker channels plus one DAPI channel) along the first axis.
- **Channel Alignment**: The pipeline enforced that the first array dimension consistently corresponded to channels. This design choice ensured that downstream routines (e.g., segmentation, intensity extraction) would refer to the same marker index across all ROIs, preventing mismatches during iterative processing.
- **Structured Storage**: Every ROI's array was stored in a dictionary keyed by the ROI identifier (e.g., image_data['ROI005'] = 22×7702×9321). This approach allowed seamless iteration over all included ROIs, regardless of potential differences in image dimensions or channel counts (although, in this HNSCC example, all kept ROIs shared the same dimensions and 22 channels).

Figure 1 illustrates the data organization for multi-channel fluorescence images across multiple ROIs. Each ROI consists of multiple stacked image channels, corresponding to different biological markers, arranged in a three-dimensional array (markers × height × width).

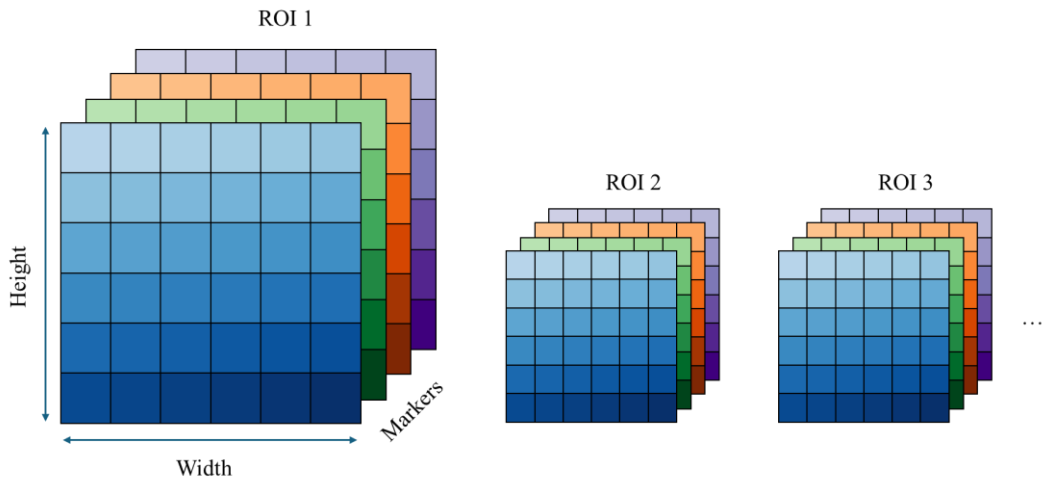

Figure 2. Data structure for multi-channel fluorescence images.

3.3 Instance Segmentation of Cells

Accurate instance segmentation is critical for single-cell analysis because it assigns a unique mask to each individual nucleus (and, by extension, each cell), ensuring that downstream quantification and spatial statistics are performed on a per-cell basis rather than on bulk tissue regions.

3.3.1 Choosing the Nuclei Segmentation Marker: DAPI

DAPI reliably labels cell nuclei, providing a robust spatial anchor for segmentation in complex tissue environments [23]. In the generic workflow, the DAPI channel is extracted from the multi-channel image stack and passed to the segmentation algorithm. For the HNSCC example, nuclei were delineated on the high-contrast DAPI channel (channel 14), which exhibited uniform fluorescence across all retained ROIs. This choice guarantees that segmentation boundaries correspond precisely to nuclear morphology, forming the foundation for subsequent cytoplasmic expansion and marker quantification.

3.3.2 Nuclei segmentation with Cellpose Integrated in QuPath

Cell segmentation was carried out using QuPath [18] and open-source software for digital pathology by applying the integrated segmentation algorithm Cellpose [19] to each HNSCC ROI. First, the DAPI channel was extracted from the multi-channel image stack and provided as the sole input for nuclear detection. Cellpose was then configured using a single, harmonized parameter set for all ROIs (see Table 5 for details). In this configuration, the model was set to "Cyto3," pixel size locked at 0.17 µm, flow threshold at 0.4, cell probability threshold at 0.0, and estimated diameter fixed at 60 px (≈10 µm).

Table 5. Optimized Cellpose parameters for nuclear segmentation.

Parameter	Final value	Rationale
Model	Cyto3	Empirically yielded best generalization to densely packed epithelium.
Pixel size	0.17 µm	Matches metadata; prevents size distortion.
Detection channel(s)	Channel 14 (DAPI)	High SNR for nuclear boundaries.
Median diameter	60 px	≈ 10 µm; tuned on a subset of ROIs.

3.3.3 Cytoplasm Estimation by Nuclear Boundary Expansion

Although DAPI-based segmentation yields accurate nuclear outlines, many biomarkers of interest (e.g., CD163, CD11b, PD-L1) localize to the cytoplasm or cell membrane rather than the nucleus. To ensure proper attribution of these signals, a cytoplasmic estimation strategy expands each segmented nuclear boundary outward by a predefined radius.

This morphological expansion generates an approximate "whole-cell" mask, capturing the perinuclear and cytoplasmic compartments necessary for reliable intensity measurements. In this study, a 3-px expansion was chosen based on visual inspection in QuPath, striking a balance between capturing membrane marker signal and avoiding overlap with adjacent cells. Once parameters were specified, batch processing was executed, producing a labeled mask for each ROI in which every segmented nucleus—and its expanded cytoplasmic region—received a unique integer identifier.

In Figure 3, image A displays the raw DAPI channel, where DAPI is green and cleanly marks each nucleus. In image B two concentric red contours are super-imposed on exactly the same field of view:

- The **inner red line** traces the nuclear boundary returned by Cellpose.
- The **outer red line** is produced by uniformly expanding every nuclear mask by a user-defined radius (3 px in this study) yielding an approximate cytoplasmic/perinuclear boundary.

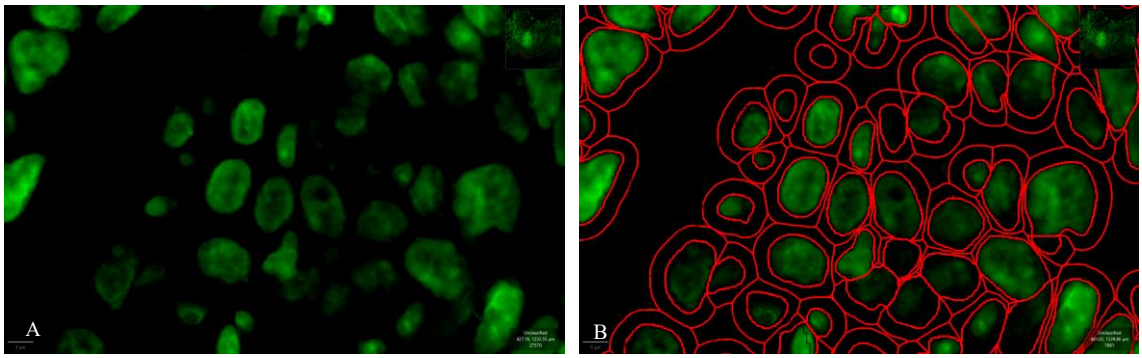

Figure 3. Cytoplasmic estimation by morphological expansion of 3px around DAPI-segmented nuclei.

To illustrate how cytoplasmic expansion enables precise biomarker attribution, Figure 4 presents four example overlays on the same cell. In panel A, the green channel shows DAPI-stained nuclei, and the red contour marks both the original Cellpose nuclear outline and its uniformly expanded cytoplasmic boundary. Panel B adds a magenta Ki-67 channel—because Ki-67 is a nuclear proliferation marker, its signal (magenta) overlaps the DAPI (green) inside the inner contour. Panel C shows the yellow NGFR channel; NGFR is cytoplasmic, and its signal falls in the expanded region between the inner and outer red contours, demonstrating accurate assignment to that cell. Finally, panel D merges all three markers (green DAPI, magenta Ki-67, yellow NGFR) with dual red outlines, confirming that each biomarker is correctly localized to the nucleus or cytoplasm of the same segmented cell.

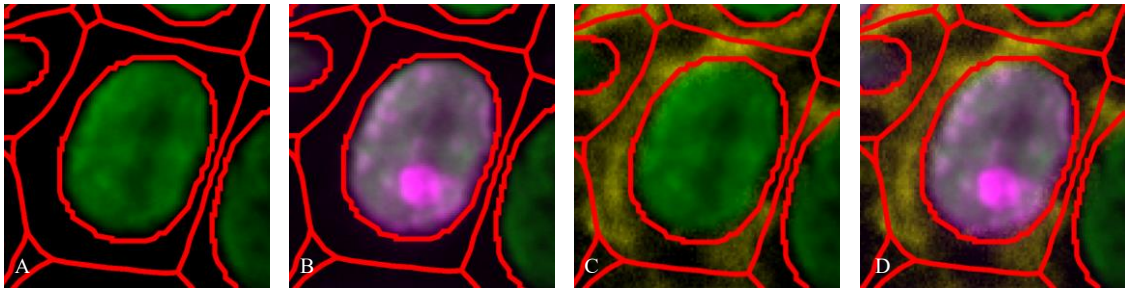

Figure 4. Cytoplasmic expansion enables cell-specific biomarker mapping.

3.3.4 Output: Labeled Mask

After segmentation and cytoplasmic region estimation, the pipeline generates a final labeled-mask image (Figure 5). In panel A, the red contours (inner and outer) are overlaid on the original DAPI channel to show the segmented nuclei and their uniformly expanded cytoplasmic boundaries. Panel B displays the same regions as a pseudo-colored label mask, where each cell has been assigned a unique integer ID and rendered in a distinct color; background pixels (ID = 0) remain black.

This labeled mask serves as a critical reference for all downstream quantitative analyses. Each unique cell label anchors marker intensity extraction, cell classification, and spatial measurements, ensuring that fluorescence signals and positional attributes map unambiguously back to individual cell entities within the original images.

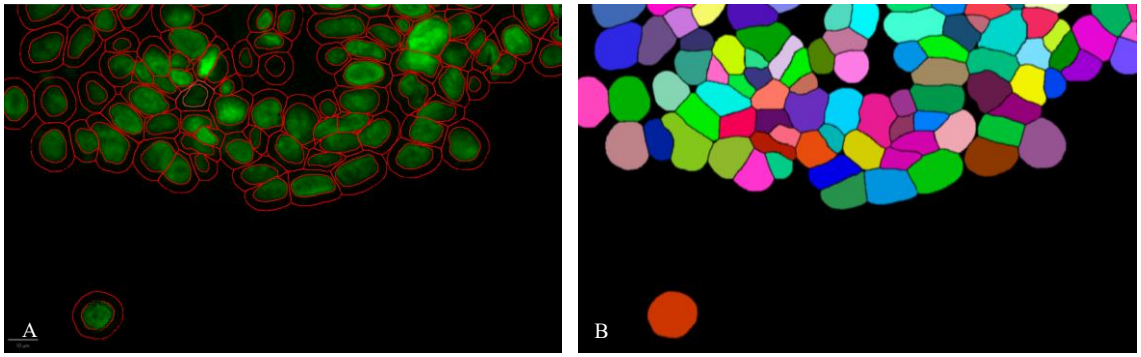

Figure 5. Pseudo-colored labeled mask: each segmented cell is uniquely colored (IDs 1–n) and background pixels (ID 0) are black.

3.4 Marker Intensity Extraction per Cell

After segmentation and annotation of cells with their spatial identities the pipeline extracts quantitative measurements of fluorescence intensity data for each segmented cell and each fluorescent marker. This process is fundamental, as it determines marker expression levels within individual cells, facilitating the cell population classification and the downstream analyses of spatial distributions, and proximity measurements. The following describes the pipeline steps in detail:

3.4.1 Intensity Extraction and Measurement

The pipeline iterates over the labeled cell mask generated during segmentation. Each cell is uniquely identified by an integer value, distinguishing it from the background (assigned with a value of zero). For each identified cell, pixel intensities from every fluorescence channel corresponding to distinct biological markers (e.g., CD3, CD16, cytokeratin) are independently extracted from the original multi-channel image.

Subsequently, the mean intensity is calculated for each marker within each cell. This statistical measure, defined as the average of all pixel intensities in the cell's segmented region, captures expression variations across the cellular population. While the mean intensity is the default metric, alternative measures such as median or sum may be used depending on specific analytical requirements. Figure 6 shows how after segmentation the pipeline extracts the mean intensity of each fluorescence channel for a given "Cell 1". The segmented multichannel image (red contour) is split into five marker channels, and

for each channel the pipeline computes the mean pixel intensity *μ_intensity, cell_1, marker_i*.

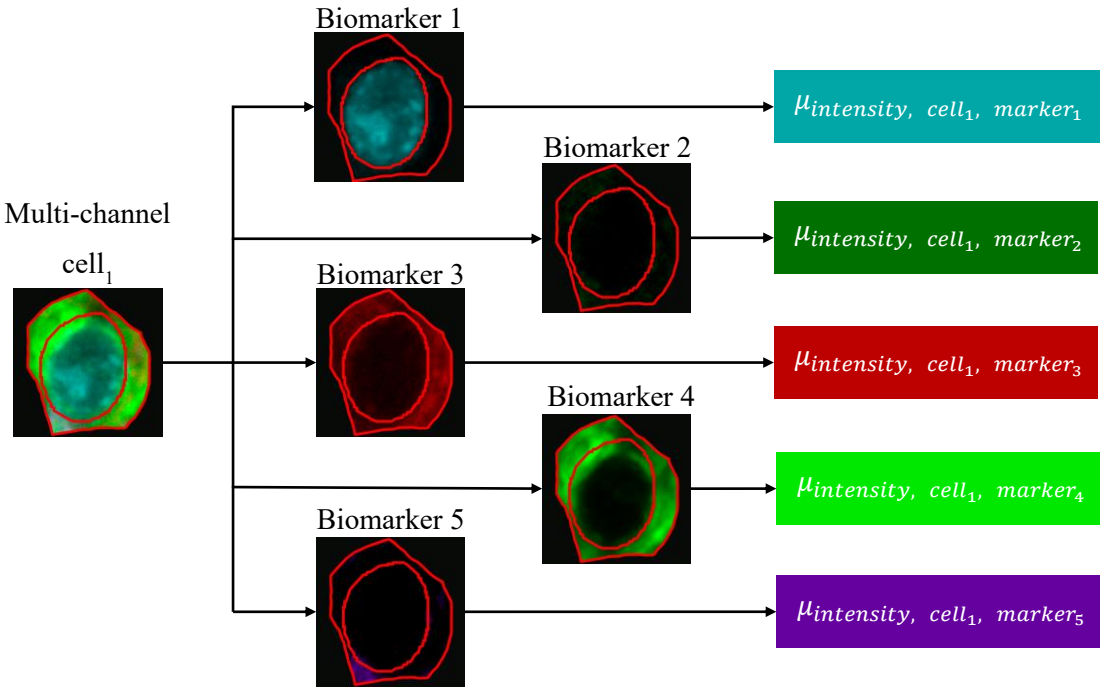

Figure 6. Mean fluorescence-marker intensity extraction for a given cell.

3.4.2 Marker Intensity Table Construction

Following fluorescence intensity extraction and measurement, the pipeline consolidates the calculated mean intensities into a structured data table. This table is organized with each row representing a unique cell, identified by a combination of the ROI and the cell ID from the segmentation mask. Each marker is represented as a distinct column within this table, containing the mean intensity value calculated for each cell.

Additional features for single-cell characterization, such as cell area (expressed in pixels and calibrated units, e.g., square micrometers), is also included.

Table 6 shows a snapshot of this per-cell dataset. Note that this is an illustrative example containing only three markers (CK positivity, CD3, and Ki67) across three cells. The "Mean Intensity CD3" and "Mean Intensity Ki67" columns contain the fluorescence mean values that will later be compared against adaptive thresholds to call positivity.

Table 6. Illustrative per-cell mean-intensity table showing cytokeratin (CK) status and mean fluorescence for CD3 and Ki67.

ROI	DAPI ID	Area µm2	Centroid y	Centroid x	Mean Intensity CD3	Mean Intensity CD4	Mean intensity Ki67
ROI 1	101	160.19	5 584.58	5 031.40	153.67	173.57	154.04
ROI 1	102	170.63	2 198.46	3 141.80	199.20	247.66	251.39
ROI 2	101	135.80	550.27	7 322.03	92.53	324.21	259.41
…	…	…	…	…	…	…	…

3.5 Adaptive-Thresholding for Tumor Masks and Cell Marker Positivity

A single adaptive-threshold formula is applied both to generate tissue masks (tumor vs. stroma via cytokeratin (CK), and NGFR sub-compartments) and to classify each cell as positive or negative for individual markers. The steps below describe how background considerations inform the choice of threshold parameters, then detail mask generation and marker-level positivity calls.

3.5.1 Background and Noise Considerations

Fluorescence images invariably contain non-specific signal from sources such as autofluorescence, scattered light, or low-affinity antibody binding. Relying on a fixed global cutoff often misclassifies background pixels (or low-signal cells) as true positive. An adaptive threshold—calculated per marker using summary statistics of the intensities—adjusts for marker-specific background heterogeneity [22]:

$$T_{marker} = \mu_{marker} + k \cdot \sigma_{marker}$$

where μ_{marker} and σ_{marker} are the per-pixel mean and standard deviation of intensities in the marker channel, and k is a scaling factor (0–3) that adjusts threshold stringency based on background staining. For markers with minimal nonspecific signal (e.g., CK), setting $k = 0$ (i.e., threshold at the global mean) cleanly separates true epithelial signal from background. For markers with heterogeneous or weak staining (e.g., NGFR or CD3), a nonzero k is assigned per ROI to avoid under- or over-segmentation.

Figure 7 illustrates two scenarios of marker staining: A depicts clean nuclear Ki67 staining (magenta), exhibiting distinct positive nuclei against a non-fluorescent background, simplifying threshold definition. In contrast, B demonstrates diffuse FoxP3 staining (red), with extensive non-specific background that necessitates a stringent threshold selection to accurately delineate true positive cells.

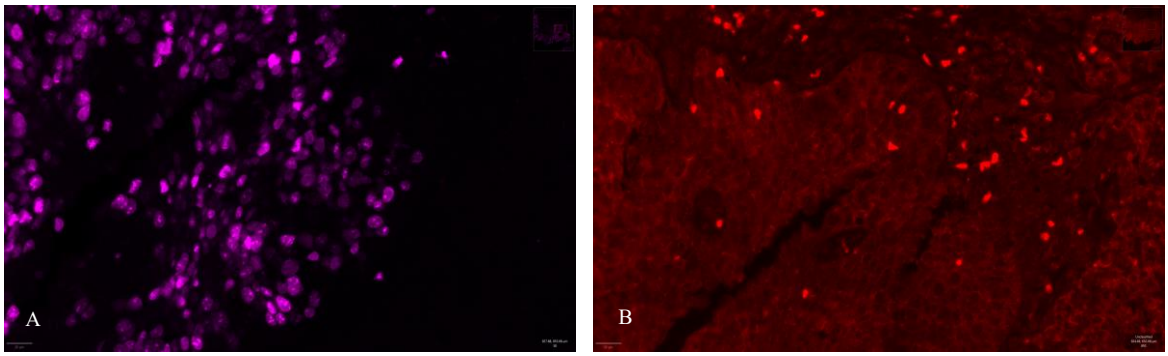

Figure 7. (A) Clean nuclear Ki67 staining (magenta) with no background. (B) FoxP3 staining (red) showing diffuse background; only the brightest spots correspond to true positives.

3.5.2 CK-Based Tumor Mask

1. **Threshold Selection**
    - Compute μ_{CK} and σ_{CK} for each ROI's CK channel.
    - Since CK exhibits very low background, choose $k = 0$, so $T_{CK} = \mu_{CK}$.
2. **Initial Binary CK Mask**
    - Label pixels with CK intensity $\geq \mu_{CK}$ as tumor (1); others as stromal (0).
3. **Morphological Refinement**
    - **Remove Small Objects**: Delete connected components < 2 000 px² to eliminate debris or antibody precipitates.
    - **Fill Small Holes**: Fill holes ≤ 10 000 px² to seal intracytoplasmic gaps and produce a contiguous tumor region.
4. **Final CK Mask**
    - Pixels = 1 denote CK^+ tumor area; pixels = 0 denote non-tumor stroma.

- Figure 8A shows the original CK channel, Figure 8B the provisional mask after thresholding, and Figure 8C the post-processed mask.

Cells whose centroids fall within this CK mask are labeled "tumor-associated," while those outside are labeled "stromal."

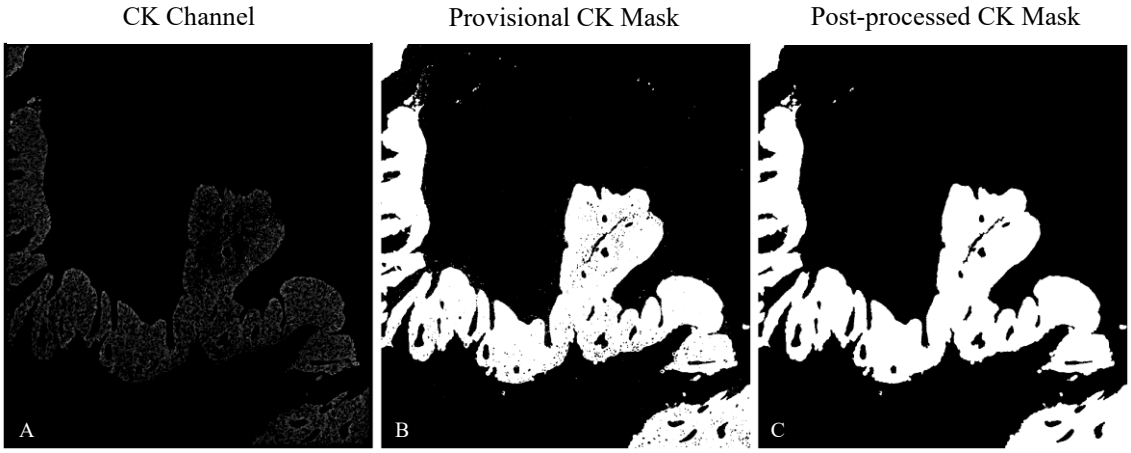

Figure 8. Example workflow for CK-based tumor mask generation.

3.5.3 NGFR-Based Sub-Compartment Mask

For NGFR, the same adaptive-threshold workflow is applied as for CK—first calculating $T_{NGFR} = \mu_{NGFR} + k \cdot \sigma_{NGFR}$, then converting pixels above this threshold to 1 ($NGFR^+$) and those below to 0. Because NGFR staining was weaker and more heterogeneous, each ROI was assigned a specific k_{NGFR} value (Table 7) to ensure neither under- nor over-segmentation. Once thresholded, the binary NGFR mask undergoes the identical morphological post-processing steps used for CK (small-object removal and hole filling) to eliminate noise artifacts and produce a contiguous $NGFR^+$ region. Cells whose centroids lie within this refined mask are designated as $NGFR^+$ tumor cells, while those outside are $NGFR^-$ or non-epithelial.

Table 7. ROI-specific scaling factors used for NGFR thresholding.

ROI file	k_{NGFR}
ROI5	1.8
ROI6	1.8
ROI7	1.5
ROI8	1.2
ROI11	2.4
ROI13	2.1

3.5.4 Marker Positivity Calls per Cell

Using the per-cell mean-intensity table (Table 6), each marker's global mean and standard deviation are computed across all cells. A predefined scaling factor k is then applied to adjust threshold stringency based on each marker's background characteristics.

Table 8 lists the channel-wise scaling factors used to derive the binary master table (Table 9) of the HNSCC study. As explained in Section 3.5.1, lower k values correspond to channels with minimal background (e.g. Ki-67), whereas higher values compensate for greater noise or staining heterogeneity (e.g. PD-L1, CD8α).

Table 8. Global scaling factors *k* for marker-specific positivity calls.

Marker (channel)	$k_{Markers}$
NGFR (mean intensity)	0.25
Ki-67	0.00
PD-L1 (CD274)	2.50
IFN-γ	1.50
FOXP3	2.25
CD3	1.25
CD4	1.00
CD8α	2.50
CD68	2.00
CD11b	2.00
CD11c	2.00
HLA-DR	1.50

3.5.5 Master Binary Intensity Table

Following application of marker-specific thresholds a comprehensive, cell-by-cell binary matrix is assembled. For every cell and every marker, if the cell's mean intensity meets or exceeds that marker's threshold, it is assigned a value of 1 ("positive"); otherwise, it is assigned 0 ("negative"). These binary calls are appended as new columns (e.g., CD3_binary, Ki67_binary) in the master table. This resulting table—containing spatial/morphological metadata alongside one 0/1 column per marker—serves as the foundation for all downstream phenotypic definitions and analyses.

The columns in the master table include spatial and morphological cell features (e.g. cell area in μm², centroid coordinates) followed by one binary column per marker (e.g. CK, CD3, Ki-67). An illustrative extract is shown in Table 9. Only three markers are displayed

here for clarity, but any number of markers can be included. This Boolean encoding ensures that downstream routines can efficiently filter or group cells based on arbitrary combinations of marker expressions.

Table 9. Illustrative binary master table of per-cell positivity calls for CK, CD3 and Ki-67.

ROI	DAPI ID	Area µm2	Centroid y	Centroid x	Positivity CK	Positivity CD3	Positivity Ki-67
ROI 1	101	160.19	5 584.58	5 031.40	1	0	0
ROI 1	102	170.63	2 198.46	3 141.80	1	0	1
ROI 2	101	135.80	550.27	7 322.03	0	1	1
…	…	…	…	…	…	…	…

3.6 Cell Phenotype Definition and Counting

Identifying specific cell phenotypes in complex tissue samples requires combining binary marker-positivity calls (0/1) into logical rules that define each subpopulation. Once defined, the pipeline quantifies the number and proportion of cells in each phenotype per ROI. Below, the general approach is outlined and then illustrated with exact phenotype definitions used in the HNSCC experiment.

3.6.1 Defining Subpopulations via Boolean Logic

All per-cell positivity calls (columns such as CD3_binary, CD4_binary, FOXP3_binary, CD8α_binary, CD68_binary, CD11b_binary, CD11c_binary, HLA-DR_binary, etc.) reside in the "master binary intensity table" (Table 9). A cell subpopulation is defined by a logical conjunction (AND) of one or more of these binary columns equaling 1 (and, where needed, others equaling 0).

For the HNSCC study, seven mutually exclusive immune classes (plus a nested "Activated CD8 T cell" subset) were specified (Table 10). Each rule combines marker positivity to capture a distinct phenotype.

Table 10. Marker-Specific Positivity Rules for Immune Phenotypes.

Phenotype	Logical rule (marker columns = 1)
Regulatory T cells (Tregs)	CD3 ∧ CD4 ∧ FOXP3
CD8 T cells	CD3 ∧ CD8α
Activated CD8 T cells	CD3 ∧ CD8α ∧ IFN-γ
Macrophages CD68	CD68
Dendritic cells CD11b	CD11b
Dendritic cells CD11c	CD11c
Dendritic cells HLA-DR	HLA-DR

3.6.2 Tumor Characterization Counts

Beyond immune phenotypes, HNSCC epithelial heterogeneity was characterized using CK- and NGFR-based definitions. All CK^+ epithelial cells define the tumor compartment, which is sub-stratified by NGFR expression and further subdivided by functional tumor markers (Ki-67, PD-L1, IFN γ, HLA-DR). Table 11 presents the epithelial subpopulations that were counted in each ROI.

Table 11. Tumor Characterization Subpopulations (HNSCC).

Tumor Characterization (CK^+)	
$NGFR^+$	**$NGFR^-$**
Tumor (CK^+)	
Tumor $NGFR^+$	Tumor $NGFR^-$
Tumor $NGFR^+$ $Ki67^+$	Tumor $NGFR^-$ $Ki67^+$
Tumor $NGFR^+$ $CD274^+$	Tumor $NGFR^-$ $CD274^+$
Tumor $NGFR^+$ IFN^+	Tumor $NGFR^-$ IFN^+
Tumor $NGFR^+$ HLA DR^+	Tumor $NGFR^-$ HLA DR^+

3.6.3 Tumor-Infiltration Counts

To evaluate immune cells tumor infiltration, immune cell populations are counted separately within CK^+ tumor regions and CK^- stroma. For each immune phenotype defined in Table 12:

- **Tumor (Intratumoral):** Centroid lies within the CK mask (CK_binary = 1).
- **Stroma (Stromal):** Centroid lies outside the CK mask (CK_binary = 0).

Considered cell populations for tumor-infiltration counts are presented in Table 12.

Table 12. Tumor Infiltration Subpopulations (HNSCC).

Tumor Infiltration	
Tumor (CK^+)	**Stroma (CK^-)**
Tumor $CD3^+$ $CD4^+$ $FOXP3^+$	Stroma $CD3^+$ $CD4^+$ $FOXP3^+$
Tumor $CD3^+$ $CD8^+$	Stroma $CD3^+$ $CD8^+$
Tumor $CD3^+$ $CD8^+$ IFN-γ^+	Stroma $CD3^+$ $CD8^+$ IFN-γ^+
Tumor $CD68^+$	Stroma $CD68^+$
Tumor $CD11b^+$	Stroma $CD11b^+$
Tumor $CD11c^+$	Stroma $CD11c^+$
Tumor $MHCII^+$	Stroma $MHCII^+$

Counts are performed independently for each ROI. The pipeline sums the number of cells satisfying each logical rule to generate absolute infiltration counts per phenotype in tumor versus stroma. Although the counts are absolute, the total number of cells is also provided so ratios (e.g., tumor vs. stroma percentages) can also be calculated.

3.6.4 Tumor-Infiltration Counts Related to NGFR Expression

To assess how immune cells distribute relative to NGFR status within the tumor, CK^+ cells are subdivided into $NGFR^+$ and $NGFR^-$ compartments, and the same immune-phenotype rules are applied within each sub-compartment. Considered cell subpopulations for NGFR-related infiltration counts are presented in Table 13.

Table 13. Tumor Infiltration Related to NGFR.

Tumor Infiltration Related to NGFR (CK^+)	
$NGFR^+$	**$NGFR^-$**
Tumor $NGFR^+$ $CD3^+$ $CD4^+$ $FOXP3^+$	Tumor $NGFR^-$ $CD3^+$ $CD4^+$ $FOXP3^+$
Tumor $NGFR^+$ $CD3^+$ $CD8^+$	Tumor $NGFR^-$ $CD3^+$ $CD8^+$
Tumor $NGFR^+$ $CD3^+$ $CD8^+$ IFN-γ^+	Tumor $NGFR^-$ $CD3^+$ $CD8^+$ IFN-γ^+
Tumor $NGFR^+$ $CD68^+$	Tumor $NGFR^-$ $CD68^+$
Tumor $NGFR^+$ $CD11b^+$	Tumor $NGFR^-$ $CD11b^+$
Tumor $NGFR^+$ $CD11c^+$	Tumor $NGFR^-$ $CD11c^+$
Tumor $NGFR^+$ $MHCII^+$	Tumor $NGFR^-$ $MHCII^+$

3.7 Visualization and Quality Control

Effective visualization is essential for verifying that the phenotyping and cell counts derived by the pipeline accurately reflect the underlying biology. Our approach incorporates two complementary visualization strategies: quantitative bar plots that

summarize cell counts per cell population and a comprehensive, multi-panel imaging module to inspect cell type classification.

3.7.1 Quantitative Bar Plots for Cell Population Counts

Cell counts are displayed as bar plots, with the x-axis listing ROIs and the y-axis showing cell counts (often on a log scale to accommodate large range differences). Each bar represents a single subpopulation count in that ROI and is labeled with its numeric value. By plotting all subpopulations side by side for each ROI, users can quickly compare relative abundances across samples and identify any outliers or unexpected patterns.

3.7.2 Image-Based Overlay Visualization for Subpopulation Verification

To validate that automated phenotype assignments match actual fluorescence signals at the single-cell level, each ROI is processed to produce an eight-panel figure. Figure 9 demonstrates this workflow specifically for the CK^+ $CD3^+$ subpopulation. Panels are arranged in two rows (A1–D1 on top, A2–D2 on bottom) and defined as follows:

1. **Top Row – Raw Channels and Individual Views:** This row displays the unprocessed channel data (CK and CD3) and two summary images. For the CK^+ $CD3^+$ example, the panels appear in this order:

    - **Figure 9A1: Raw Composite (CK + CD3):** Shows the unaltered CK channel in red and CD3 channel in green exactly as acquired. This composite reveal both markers "as is," enabling visual assessment of raw CK and CD3 distributions simultaneously.
    - **Figure 9B: CK Binary Mask Visualization:** Displays the binary CK mask that was previously generated (white = CK^+, black = background).
    - **Figure 9C1: CD3 Intensity Map Visualization:** Presents the pre-existing CD3 intensity image in normalized grayscale.
    - **Figure 9D1: Mean Intensity Overview:** Shows the same CK + CD3 composite as A1 but rendered in grayscale. Although D1 does not add new information, it provides a black-and-white reference that can be directly

compared to D2 (which includes cell overlays) to verify channel alignment.

2. **Bottom Row – Segmentation Overlays and Subpopulation Highlighting** After displaying the masks and intensity maps above, this row demonstrates how those thresholds apply to segmented cells:

    - **Figure 9A2: Composite + Segmentation Overlays:** Re-renders the CK + CD3 composite from A1, now with all segmented-cell outlines superimposed in distinct colors.
    - **Figure 9B2: CK^+ Cell Overlay:** Highlights only those segmented cells that satisfy CK_binary = 1 (determined previously). CK^- cells remain faint. This panel verifies that every CK^+ cell is accurately identified.
    - **Figure 9C2: $CD3^+$ Cell Overlay:** Highlights only the segmented cells for which CD3_binary = 1 (based on the earlier intensity threshold). $CD3^-$ cells are shown faintly. This panel confirms that $CD3^+$ cells align with the true CD3 signal.
    - **Figure 9D2: CK^+ & $CD3^+$ Cell Overlay:** Highlights only those cells satisfying both CK_binary = 1 and CD3_binary = 1. All other cells appear dimmed. This final panel confirms that the CK^+ $CD3^+$ intersection subpopulation is correctly identified.

Quick Interpretation Example:

- If a cell is highlighted in both B2 (CK^+) and C2 ($CD3^+$), it will also appear highlighted in D2.
- If a cell is highlighted in C2 ($CD3^+$) but not in D2 (CK^+ & $CD3^+$), then that cell must not be highlighted in B2 (CK^+).

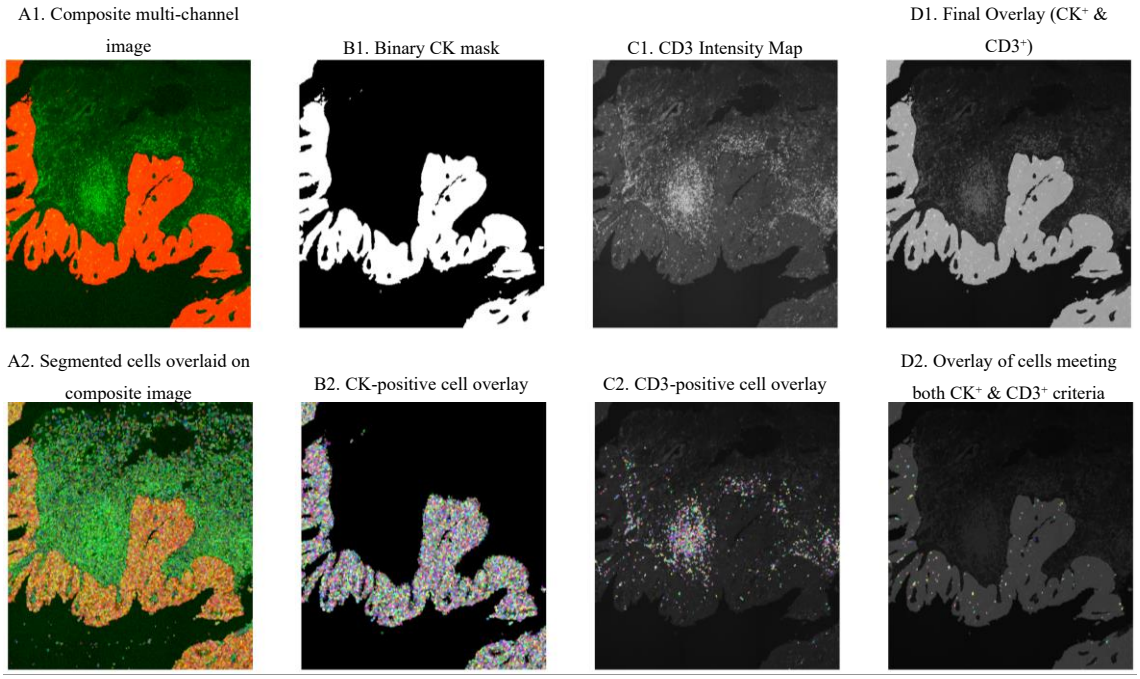

Figure 9. Multi-panel visualization of imaging, segmentation and CK^+ /$CD3^+$ subpopulation selection.

3.8 Cell population-to-Mask Distance Measurement

Once cell populations (sub-populations) have been defined (Table 10) and regional masks generated (Sections 3.5.2 and 3.5.3), quantifying each cell's proximity to a given region boundary provides a more informative measure than a simple "inside/outside" call. The sub-population-to-Mask Distance Module computes, for every cell in a chosen subpopulation, a signed Euclidean distance to the nearest point on a specified regional mask. Cells outside the mask receive positive distance values (exclusion), while cells inside receive negative values (infiltration). This continuous metric facilitates comparative analyses of cell tumor infiltration and exclusion across different populations and regions.

3.8.1 Data and Inputs

To calculate signed distances, the module requires:

1. **Regional Masks (binary)** – For each ROI, the tissue regions of interest (e.g., CK^+ tumor, $NGFR^+$ sub-compartment) are represented as binary images (pixels = 1

inside the region, 0 outside). These masks were produced as described in Section 3.5.

2. **Segmentation Mask (label image)** – The labeled mask from cell segmentation (Section 3.3.4) assigns a unique integer ID to each cell. From this mask, centroids (or alternative reference pixels) are extracted.

3. **Subpopulation Indicator (binary column)** – From the master table (Section 3.6), each cell's membership in the subpopulation of interest (e.g., CD8 T cells, Tregs, etc., defined in Table 10) is denoted by a binary column. Only those cells with a "1" in this column are included in distance calculations.

4. **Pixel-Size Metadata** – Physical pixel size (µm/pixel), extracted from image metadata during segmentation (Section 3.3.2), ensures that all computed distances are expressed in micrometers.

3.8.2 Generation of the Continuous Distance Map

For a given binary regional mask, a continuous distance map is constructed in two steps:

1. **Distance Outside the Region**: A Euclidean distance transform is applied to every pixel outside the mask to compute its distance to the nearest mask boundary. Pixels immediately adjacent to the boundary have a distance of 1 (pixel unit), and distances increase for pixels farther away.

2. **Distance Inside the Region**: A second Euclidean distance transform is applied to pixels inside the mask (i.e., treating the mask interior as the "outside" for this step) to compute how far each interior pixel is from the boundary. Those interior distances are then multiplied by –1 to assign negative values (indicating infiltration).

Combining the two transforms yields a single continuous distance map in which:

- Pixels on the boundary = 0 distance
- Pixels outside the region = positive distance (exclusion)

- Pixels inside the region = negative distance (infiltration)

Figure 10 shows a simplified example of how the signed distance is calculated for each cell relative to a specified region. In this panel, the selected region (e.g., a CK^+ tumor mask) is rendered in light blue with a solid blue outline marking its boundary. Black dots represent individual cells from the chosen subpopulation. For a cell located outside the region, the red dashed line illustrates the positive Euclidean distance from the cell's centroid to the nearest point on the region boundary. Conversely, for a cell inside the region, the green dashed line indicates the negative Euclidean distance from its centroid to the boundary. This visualization makes clear how distances transition smoothly from negative (infiltration) to positive (exclusion) values.

Once this continuous distance map is available, each cell in the selected subpopulation is assigned the signed distance corresponding to its centroid. All resulting signed distances (in μm) are then added as a new column in the master data table.

In the HNSCC dataset, two region masks are of particular interest:

- **CK Mask (Tumor Region)** – Binary mask delineating CK^+ tumor epithelium (Section 3.4.1).
- **NGFR Mask (Tumor Sub-Compartment)** – Binary mask delineating $NGFR^+$ tumor sub-regions (Section 3.4.2).

For each of the seven immune subpopulations defined in Table 10, two signed distances are recorded for every cell in that subpopulation:

- **d(CK)** – Distance to the CK mask (negative if inside CK^+ tumor, positive if outside).
- **d(NGFR)** – Distance to the NGFR mask (negative if inside $NGFR^+$ epithelium, positive if outside).

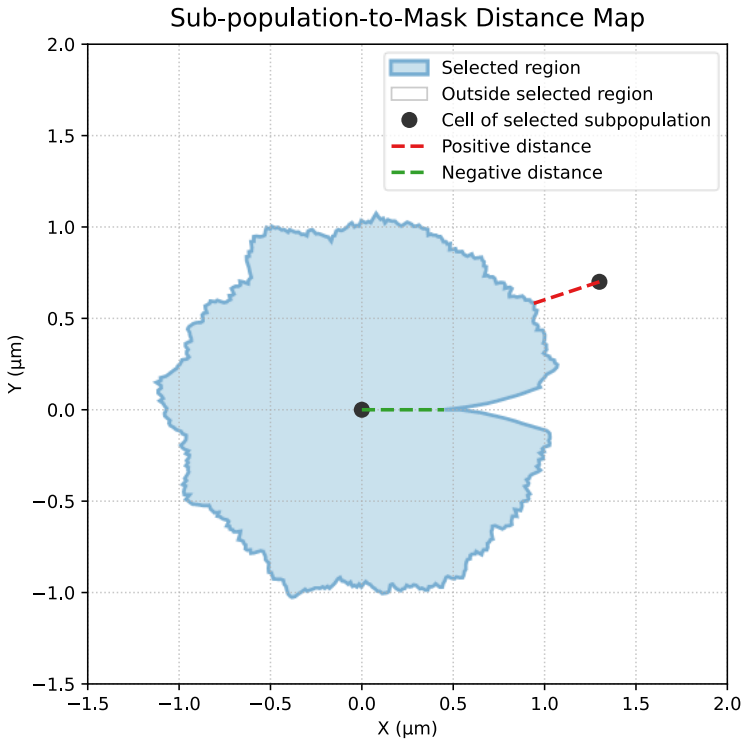

Figure 10. **Schematic of the sub-population-to-mask distance measurement.**

3.8.3 Outputs, Summaries, and Visual Validation

Once distances have been assigned to every cell in the selected subpopulation, the module produces two core outputs and an optional visualization overlay:

1. **Per-Cell Distance Attributes:** Each cell receives two signed-distance values reflecting its proximity to the CK and NGFR masks, respectively. These new columns in the master data table enable downstream statistical analyses (for example, comparing median distances across ROIs or correlating distance with marker intensity).

2. **ROI-Level Statistical Summaries:** For each ROI and subpopulation, summary statistics on the signed distances are visualized as violin-box hybrid plots to intuitively display infiltration (negative distances) versus exclusion (positive distances). All resulting per-cell distance attributes, summary tables, and distribution plots are exported as CSV and image files for downstream analyses and figure generation.

3. **Visual Validation (Color-Coded Overlay):** To verify that computed distances faithfully represent spatial relationships, a color-coded overlay of the continuous distance map can be rendered atop the original tissue image in which negative (infiltration) distances appear in green and positive (non-tumoral) distances appear in red.

3.9 Population-to-Population Distance Measurement

Following the identification and characterization of cell subpopulations based on their marker expression profiles, a critical analytical dimension involves quantifying the spatial relationships between different subpopulations within the tissue microenvironment. The Cell-to-Cell Distance Module systematically addresses this requirement by calculating detailed spatial metrics that reflect the proximity and spatial interactions between selected cell populations. Such metrics are essential for understanding biological interactions like immune cell infiltration, cellular communication, and tumor-immune dynamics.

3.9.1 Data and Inputs

To measure inter-population distances, the module requires:

1. **Segmentation Mask (label image)** – From Section 3.3.4, each cell is assigned a unique integer ID and a centroid coordinate.

2. **Cell Subpopulation Indicators (binary columns)** – From the master table (Section 3.6), each cell's membership in reference and query subpopulations (e.g., Tregs vs. epithelial cells) is flagged by a "1" in the corresponding binary column.

3. **Pixel-Size Metadata (µm/pixel)** – Extracted during segmentation (Section 3.3.2), this ensures that computed distances reflect real-world physical units.

3.9.2 Conceptual Overview and Rationale

Rather than a simple "neighbor within X µm" binary check, this module produces a precise, continuous distance for every query cell to its closest reference cell. This approach reveals subtle spatial patterns—such as clustering or exclusion—that binary

thresholds might miss. Figure 11 illustrates the concept: blue crosses denote reference cells (Subpopulation 1), red crosses denote query cells (Subpopulation 2), and purple dash-dot lines indicate the minimum Euclidean distance from each query cell to its nearest reference cell.

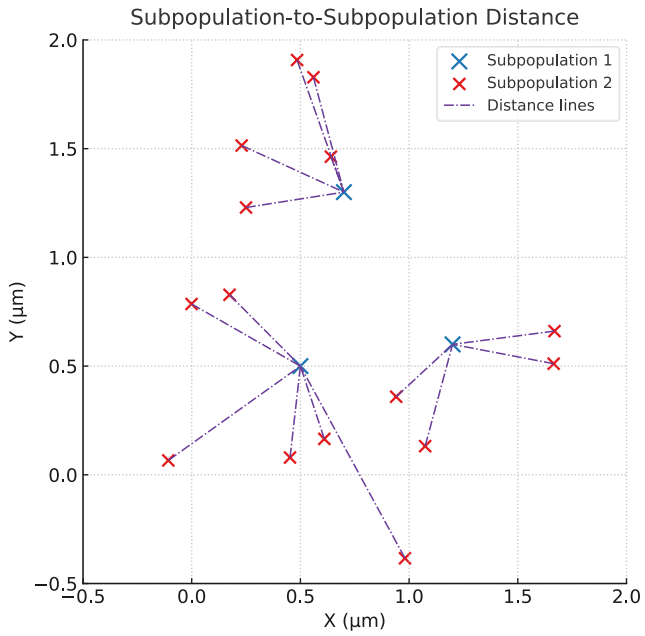

Figure 11. Conceptual schematic of subpopulation-to-subpopulation distance measurement.

3.9.3 Generation of Voronoi Diagrams for Distance Measurements

A crucial step in quantifying inter-population distances is to partition the image into "nearest-neighbor" regions around each reference cell. This is accomplished with a Voronoi tessellation based on the centroids of the reference-subpopulation cells. In practice:

1. **Extract Reference Centroids:** From the segmentation mask (Section 3.3.4), obtain the (x, y) coordinates of every cell flagged as belonging to the reference subpopulation.

2. **Construct Voronoi Tessellation:** Using these centroids, generate a Voronoi diagram over the entire ROI. Each polygonal region in this diagram contains all

points that are closer to its associated reference centroid than to any other reference centroid.

3. **Visual Validation (Schematic Example):** Figure 12 presents a simplified, schematic Voronoi overlay: blue crosses mark reference-population centroids, green dashed lines indicate the polygon edges, and the background is shown only for clarity. In an actual analysis, the same process is applied across the full image resolution, but Figure 12 makes the concept immediately clear.

Once the Voronoi diagram is established, any query cell that falls within a given polygon is guaranteed that its nearest reference neighbor is the centroid at that polygon's seed. This construction enables rapid identification of each query cell's closest reference cell without exhaustively comparing every pair.

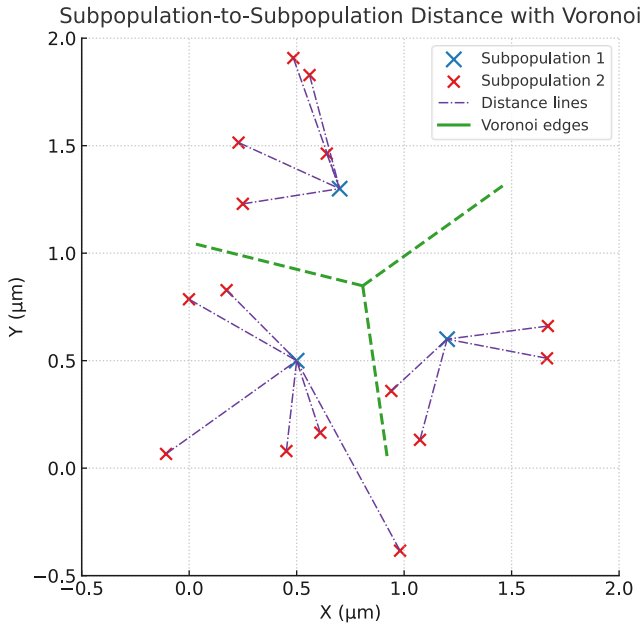

Figure 12. Voronoi tessellation of Subpopulation 1 (blue crosses) showing how each polygonal region (green edges) defines the nearest-neighbor territory around each reference cell.

3.9.4 Calculation of Inter-population Distances

With the Voronoi diagram in place, inter-population distances are calculated as follows for each query cell:

1. Identify which Voronoi polygon contains the query cell's centroid.

2. Measure the Euclidean distance (in micrometers) from the query cell centroid to the centroid of the reference cell that defines that polygon.

3. Record that distance as the cell's "distance to reference".

In the HNSCC experiment, two epithelial reference sets are considered:

- **CK^+ $NGFR^+$ cells** (reference set 1)
- **CK^+ $NGFR^-$ cells** (reference set 2)

For each reference set, the seven immune phenotypes from Table 10 (Tregs, CD8 T cells, Activated CD8 T cells, Macrophages, CD11b DCs, CD11c DCs, HLA-DR DCs) serve as query populations. In total, fourteen distance-to-reference metrics (seven immune types × two epithelial references) are computed per ROI.

3.9.5 Outputs, Summaries, and Visual Validation

Once every query cell's nearest-neighbor distance has been calculated, the module produces three main deliverables:

1. **Per-Cell Distance Attributes**: Each cell in a query subpopulation receives a new distance column indicating its micrometer-scale proximity to the designated reference set.

2. **ROI-Level Statistical Summaries**: For each ROI and each query–reference pair, summary statistics are computed. The full distance distributions are visualized using violin-box hybrid plots to reveal whether immune cells cluster close to or remain distant from their target epithelial niches.

3. **Visual Validation (Color-Coded Voronoi Overlay)**: To confirm that computed distances accurately reflect tissue spatial relationships, a color-coded Voronoi overlay is rendered on the original tissue image for each ROI and each desired subpopulation combination. In this visualization, each Voronoi polygon is shaded according to its reference cell's identity, and query cells are overlaid as dots whose

color intensity corresponds to their distance from the nearest reference cell (e.g., darker red indicates greater separation, lighter red indicates closer proximity).

3.10 Automated Detection of Tumor Invasion Fronts

3.10.1 Rationale and General Workflow

To focus the multiplex-fluorescence analysis on biologically critical regions, an independent deep-learning module was created to localize tumor-invasion fronts directly on routine Hematoxylin–Eosin (H&E) slides from HNSCC biopsies. The following bullet points summaries the successive stages:

- Slide Acquisition and Baseline Data Preparation.
- Semi-Automatic Annotation of Images.
- Data Preparation.
- Exploratory Data Analysis of the Prepared Dataset.
- Network Architecture.
- Training Procedure.
- Inference Pipeline and Post-Processing.
- Overlay Generation and Metric Evaluation.

3.10.2 Slide Acquisition and Baseline Data Preparation

Formalin-fixed paraffin-embedded (FFPE) tissue sections were stained with routine Hematoxylin–Eosin and scanned at 20 × (0.23 µm px^{-1}, 16-bit RGB) on a Panoramic 1000 slide scanner. All images retained the original color profile and optical-density values; no color normalization was applied prior to annotation in order to preserve staining variability for the data-augmentation stage.

To illustrate the starting material for our patch-and-mask workflow, Figure 13 shows a representative whole-slide H&E scan of an HNSCC biopsy. This high-resolution image captures the tumor architecture—epithelium, stroma, and surrounding tissue.

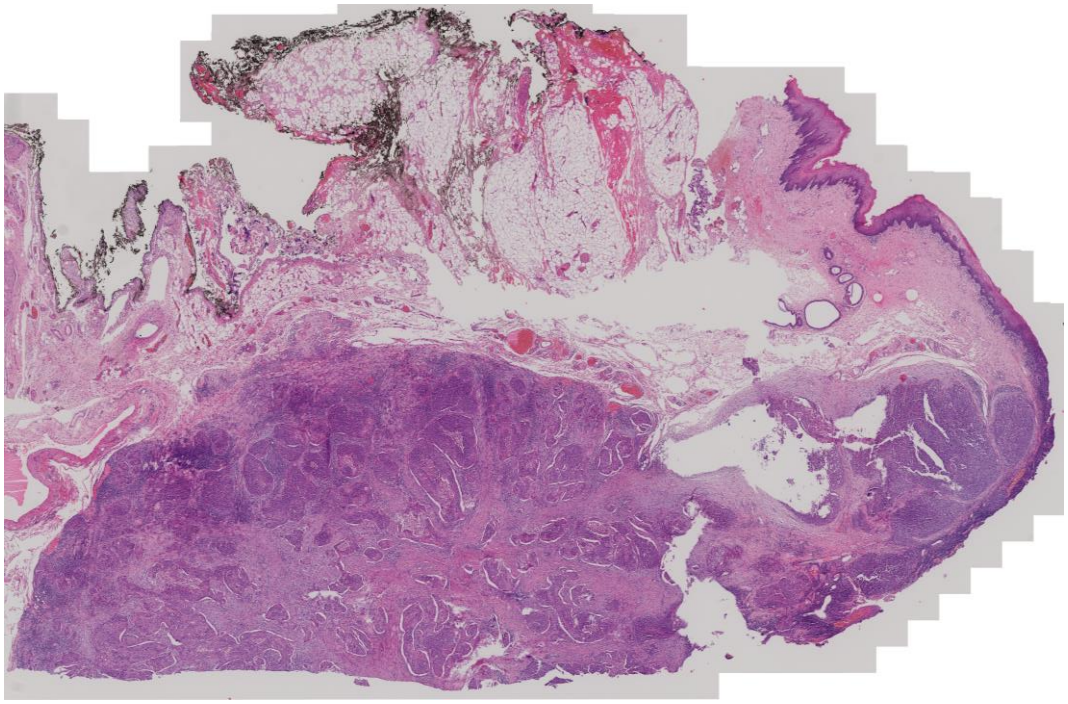

Figure 13. Representative whole-slide H&E image of an HNSCC biopsy.

3.10.3 Semi-Automatic Annotation of Images

The whole-slide images were sufficiently comprehensive to justify a dense, slide-wide annotation; however, exhaustively outlining every compartment by hand would have been extremely time-consuming. A two-stage, semi-automatic strategy was therefore adopted. First, the epithelial margin at the tumor-invasion front was delineated in QuPath 0.6.3 using free-hand polygons and supervised by a pathologist. This initial step produced a high-fidelity mask labelled invasion-front epithelium (class 1), while all remaining pixels were left unassigned.

At this stage the unlabeled pixels could correspond only to stromal tissue or background. As background is uniformly bright and stroma exhibits lower, textured intensity, an intensity-based pixel classifier was applied exclusively to the non-front area. For every unassigned pixel the mean RGB value was computed; values > 195 (8-bit scale) were classified as background (class 0), whereas all lower values were classified as stroma (class 2). The threshold of 195 was chosen empirically to sit above the 99th-percentile intensity of stromal pixels yet below the minimum intensity recorded for background across the dataset. To enforce spatial coherence, the provisional mask was post-processed

in QuPath using the Create Objects utility: both Minimum object size and Minimum hole size were set to 100 µm², thereby eliminating small debris islands and filling intraluminal gaps without altering the manually traced invasion-front contours.

This two-step procedure yielded a fully comprehensive, three-class annotation for each image. The manually traced invasion-front contours were preserved exactly as drawn, and every remaining pixel was unambiguously classified as either stromal tissue or background glass. As a result, each biopsy section achieves 100 % ground-truth coverage, providing a robust target for training the segmentation network. All of these annotations were reviewed and validated by an expert pathologist.

Figure 14 illustrates the pipeline stages: (A) the manually delineated invasion-front polygon, (B) the inverted front mask highlighting all non-front pixels, and (C) the final three-class output—red overlays denote the tumor-invasion front, yellow overlays mark background, and gray regions correspond to stromal tissue.

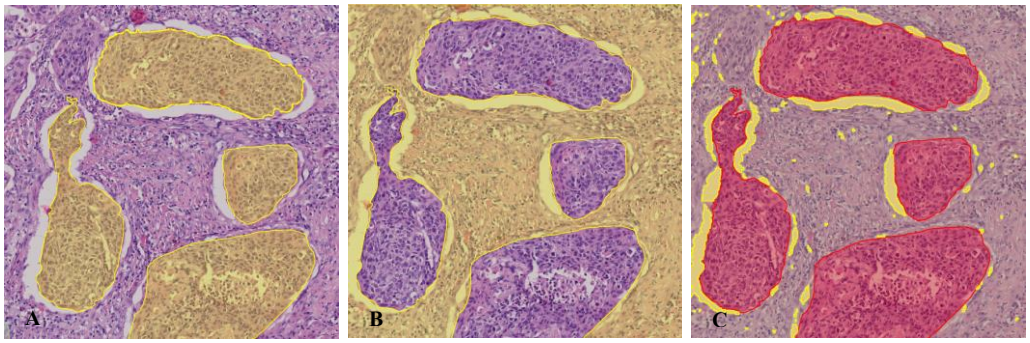

Figure 14. Semi-automatic annotation workflow: (A) manual invasion-front polygons, (B) inverted non-front mask, and (C) final three-class map.

3.10.4 Data Preparation

This subsection explains how raw whole-slide images were converted into a clean, balanced training set for the tumor-invasion-front network. The data preparation workflow is divided into the following steps:

1. **Mask rasterization and patch extraction:** Annotation polygons exported from QuPath were rasterized into a full-resolution tri-class mask perfectly aligned with the RGB slide. The slide and its mask were then subdivided into non-overlapping tiles of 2 048 × 2 048 px, a patch size chosen to be large enough to encompass

both individual cellular detail and the broader architectural context of the invasion front, yet small enough to remain computationally manageable. Each image/mask pair was saved as a lossless PNG (compression level 1) to preserve exact spatial correspondence and full intensity detail.

2. **Stain-space decomposition (H&E color deconvolution):** The RGB tile is transformed into two optical-density images that separately capture hematoxylin (nuclear detail) and eosin (cytoplasmic / stromal detail). These channels are stored alongside the original RGB patch and will provide the network with explicit stain information and improving its ability to generalize. Figure 15 shows the diagram of the stain-space decomposition process using H&E color deconvolution.

3. **Class-imbalance mitigation:** Class imbalance was addressed in two stages. First, any tile containing at least ten percent tumor was duplicated and subjected to simple random geometric transformations (90° rotations and horizontal or vertical flips) to generate additional, orientation-diverse examples of the invasion front. Then, patches made up entirely of stroma or entirely of background were removed from the corpus. These combined steps yield a more balanced set of image/mask pairs that faithfully represent each class without discarding valuable biological context.

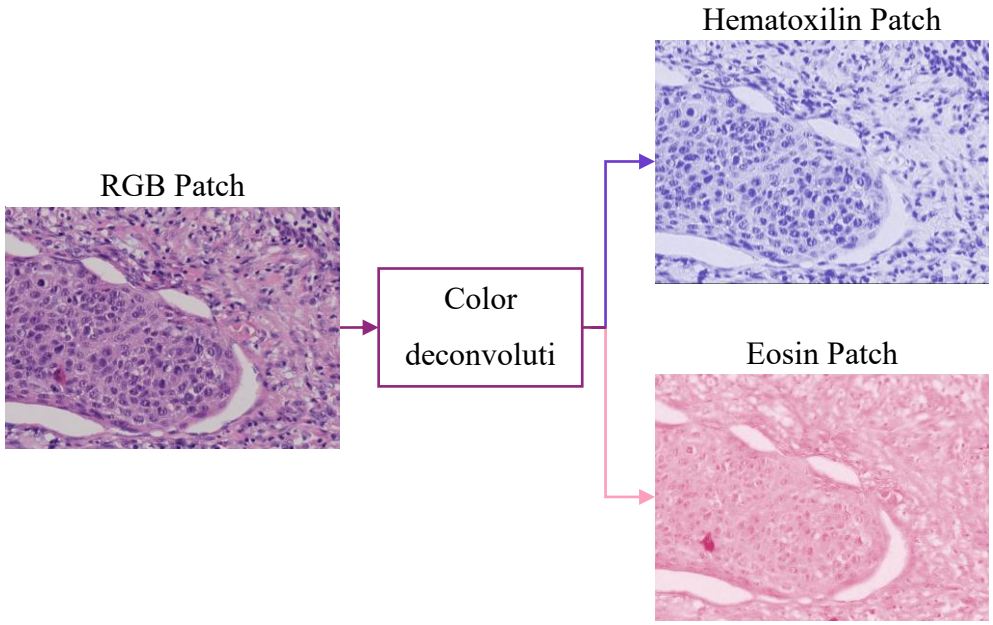

Figure 15. Stain-space decomposition of an H&E-stained RGB patch into separate hematoxylin (nuclear) and eosin (cytoplasmic/stromal) optical-density channels.

3.10.5 Exploratory Data Analysis of the Prepared Dataset

The Exploratory Data Analysis (EDA) aims to thoroughly characterize the balanced dataset prepared for training the deep-learning model that detects tumor-invasion fronts. This analysis examines class distribution, photometric properties, feature correlations, and multivariate relationships. A total of 2,003 tiles, each measuring 2,048 × 2,048 pixels, constitute the analyzed dataset.

1. Class Proportion Analysis

The dataset comprises three classes: background, front of invasion, and stroma. The average proportions across all tiles are:

- Background: 21.6% ± 30.4%
- Front of invasion: 28.0% ± 25.9%.
- Stroma: 50.4% ± 28.0%

The median values highlight a slight dominance of stromal tissue (51.1%), while the background has the lowest median proportion (5.5%). The distribution of these proportions is visualized in Figure 16, showing balanced representation with significant but controlled variability, ideal for robust neural network training.

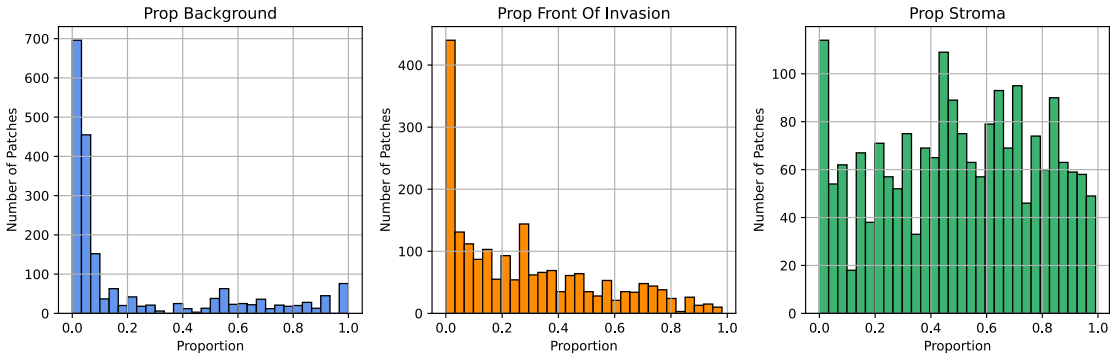

Figure 16. Histograms of tile class proportions, showing the distribution of background, invasion-front epithelium, and stroma across 2 003 patches.

2. Intensity Analysis

Photometric characterization included grayscale brightness and normalized optical density (OD) for hematoxylin and eosin stains:

- Mean grayscale brightness: 139.3 ± 30.0 (median: 129.9, range: 83.8–238.6).
- Mean hematoxylin intensity (normalized): 0.163 ± 0.042 (median: 0.168, range: 0.045–0.290).
- Mean eosin intensity (normalized): 0.189 ± 0.077 (median: 0.215, range: 0.000–0.321).

Histograms in Figure 17 illustrate single-peaked distributions for these intensities, indicating consistent staining quality and suggesting uniform scanning conditions without significant artifacts.

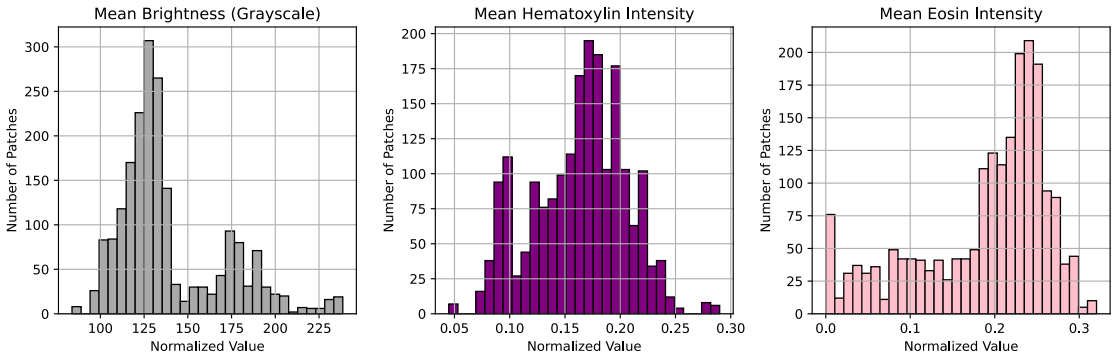

Figure 17. Histograms of mean grayscale brightness and normalized hematoxylin and eosin intensities, illustrating the consistency of staining across all tiles.

3. Correlation Analysis

Figure 18 presents the correlation matrix between features. Notable correlations include:

- Positive correlation between the proportion of front-of-invasion tissue and mean hematoxylin intensity (0.56), consistent with the higher nuclear density of invasive tumor regions.
- Moderate positive correlation between stromal proportion and eosin intensity (0.43), reflective of the eosinophilic nature of extracellular matrix-rich stroma.
- Strong negative correlations between background proportion and intensities (hematoxylin: -0.65, eosin: -0.59, grayscale: -0.61), explained by the low optical density of glass background areas.

The absence of extremely high correlations (>0.7) suggests that the features provide complementary information beneficial for network training.

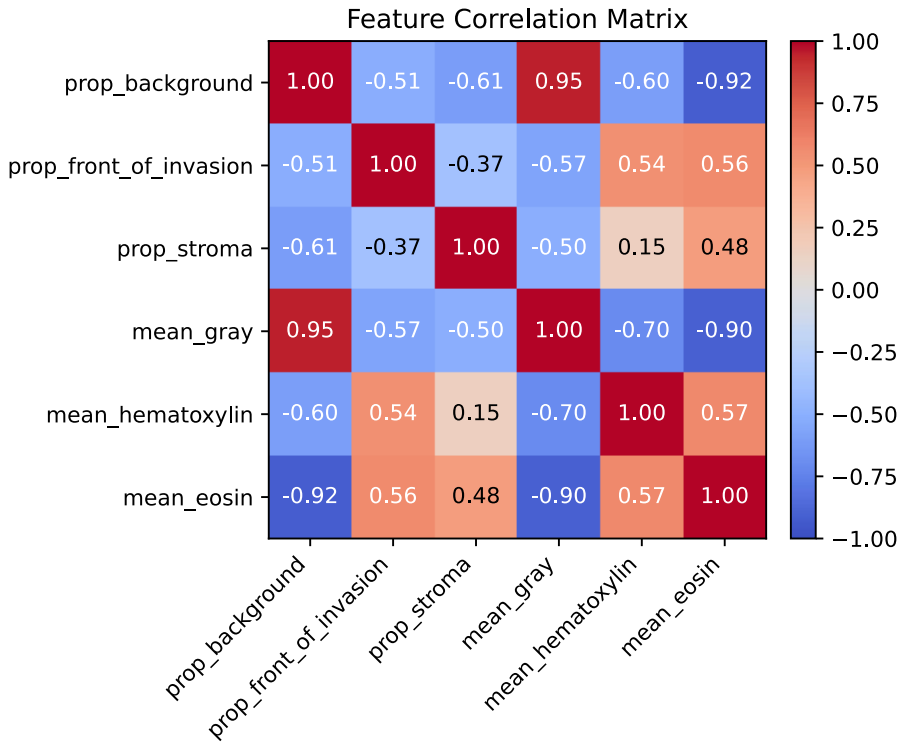

Figure 18. Annotated Pearson correlation matrix between class proportions and photometric features, highlighting positive and negative inter-feature relationships.

4. Bivariate Relationships

Scatter plots were generated to further understand the relationship between tissue proportions and stain intensities:

- Figure 19 demonstrates a clear positive trend between the proportion of front-of-invasion tissue and mean hematoxylin intensity. Regions richer in invasive tumor cells show higher nuclear staining intensities.
- Figure 20 indicates that eosin intensity increases as stromal proportion rises but then levels off in regions with very high stromal content, reinforcing the specificity of eosin staining for stromal compartments.

- Figure 21 shows that regions with a higher background proportion have higher mean grayscale brightness, reflecting the transparent nature of the background and confirming the expected photometric property of these areas.

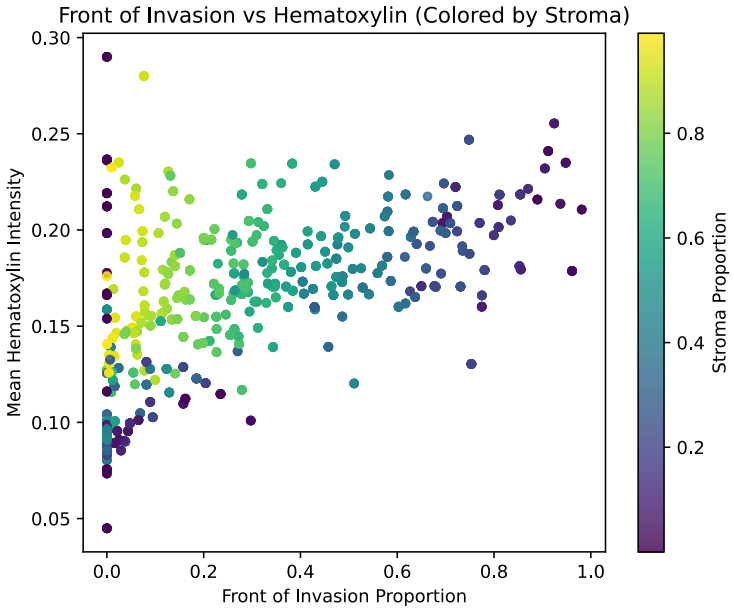

Figure 19. Scatter plot of invasion-front proportion versus mean hematoxylin intensity, with point color indicating stromal proportion.

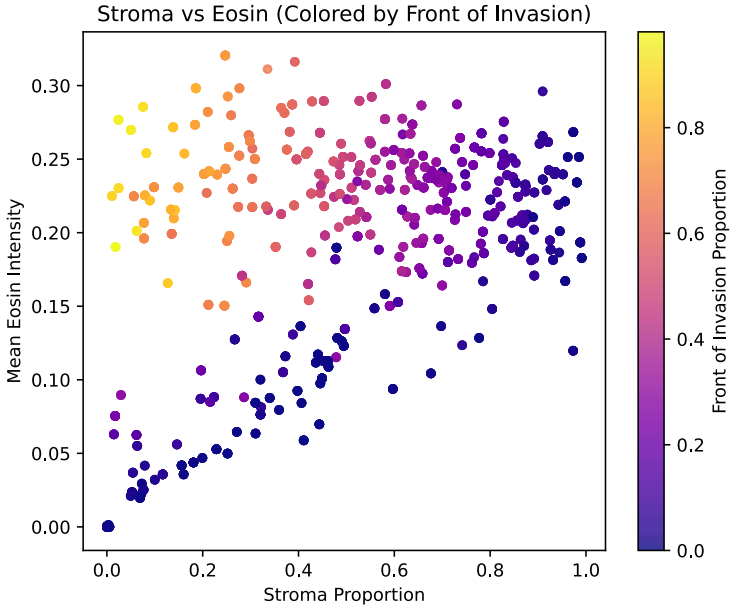

Figure 20. Scatter plot of stromal proportion versus mean eosin intensity, with point color indicating invasion-front proportion.

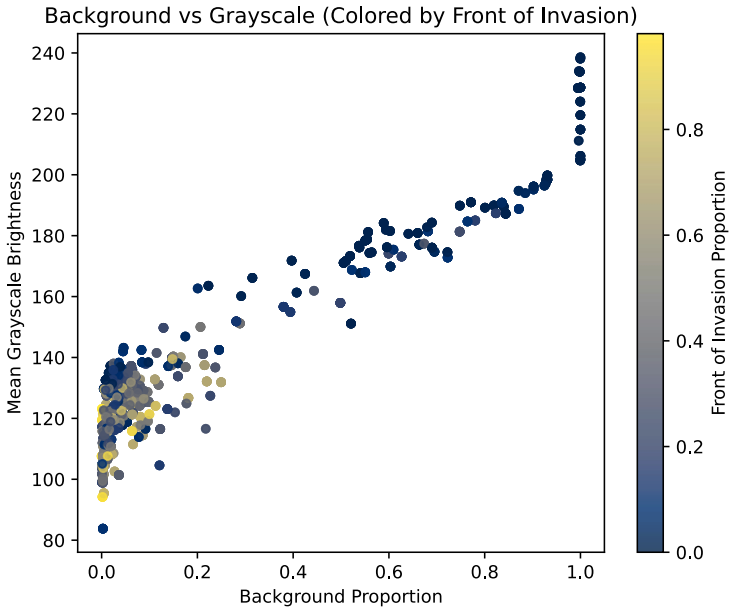

Figure 21. Scatter plot of background proportion versus mean grayscale brightness, with point color indicating invasion-front proportion.

5. Intensity Variation by Stromal Quartiles

Further analysis segmented tiles into quartiles based on stromal proportions (Figure 22). Eosin intensity progressively increases from the first quartile (lowest stromal content) to the fourth quartile (highest stromal content), confirming stromal-specific staining characteristics. Conversely, hematoxylin intensity remains relatively consistent across quartiles, emphasizing its nuclear specificity irrespective of stromal density.

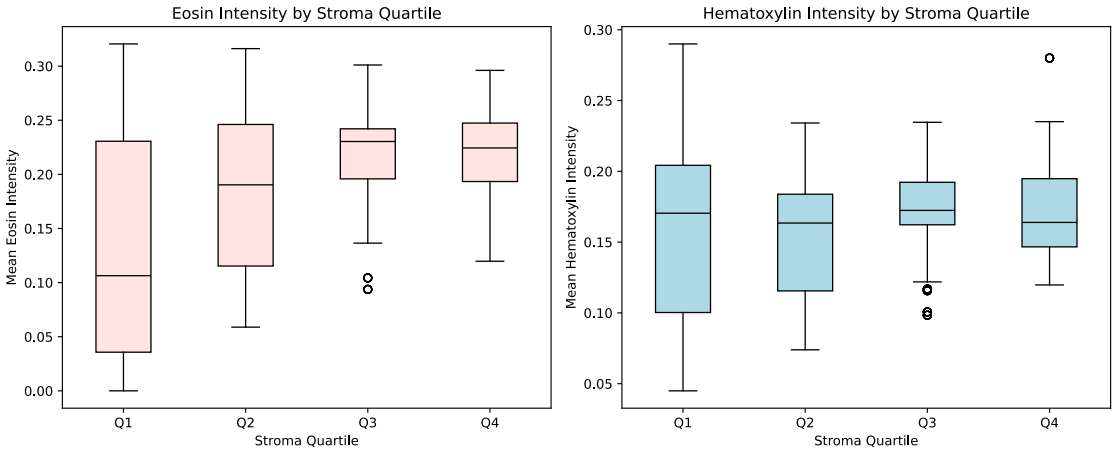

Figure 22. Box-plots of mean eosin and hematoxylin intensities stratified by stromal-proportion quartiles (Q1–Q4).

6. Multivariate Feature Overview

A comprehensive multivariate analysis (Figure 23) using pairwise scatter plots combined with kernel density estimates (KDE) reveals the clear biological separation of dominant classes within feature space:

- Background-dominated tiles occupy regions characterized by high grayscale brightness and low stain intensities.
- Tumor-front-dominated tiles cluster distinctly at higher hematoxylin intensities, demonstrating nuclear-rich staining.
- Stroma-dominated tiles bridge these groups, characterized by intermediate eosin intensities, reflective of extracellular matrix content.

These results highlight the rich discriminative power of combined intensity and proportional features for effective classification by the neural network.

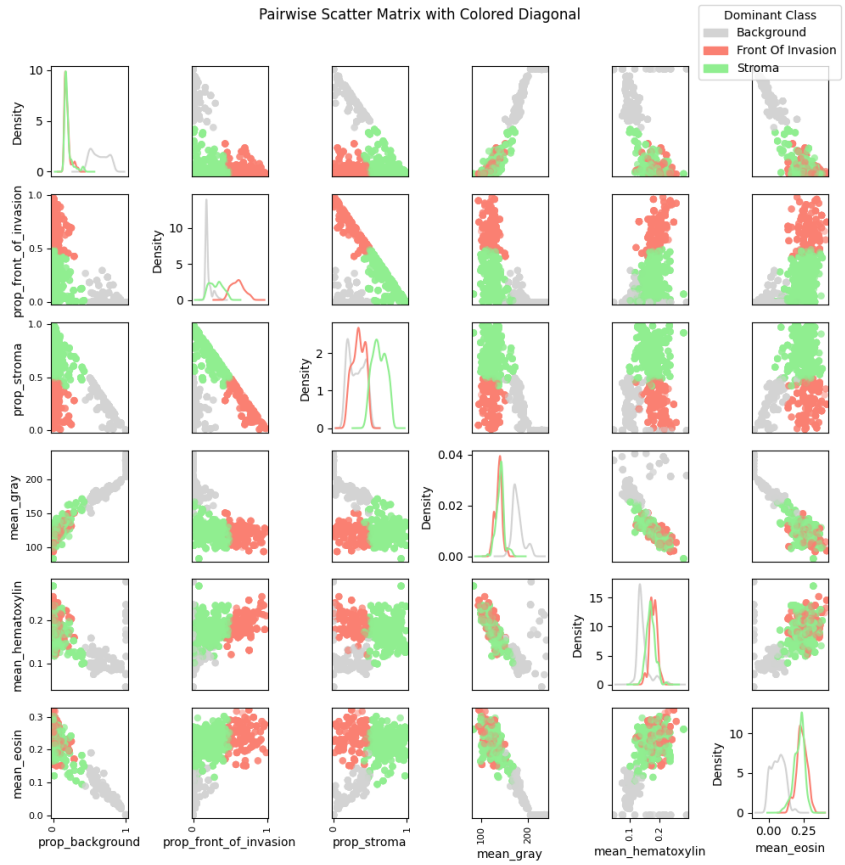

Figure 23. Pairwise scatter matrix of six key features with diagonal kernel-density estimates, colored by each tile's dominant class.

3.10.6 Network Architecture

The segmentation backbone used was a U-Net enhanced with Squeeze-and-Excitation (SE) attention blocks. Two grayscale channels—hematoxylin and eosin optical-density images—are concatenated and fed as a 2-channel tensor. With a base width of 64 filters, the model grows according to the typical U-Net doubling rule (64 → 128 → 256 → 512 → 1 024) and mirrors this hierarchy on the decoder side.

- **SE attention.** Each double convolution block ends with a channel-wise SE gate (reduction ratio = 16) that re-weights feature maps based on global context, improving class-specific saliency at little computational cost.

- **Dilated convolutions.** Dilation factors of 1, 2, and 4 are used in successive encoder stages to enlarge the effective receptive field without extra pooling, allowing the network to capture tissue architecture beyond purely cellular detail.

- **Receptive field.** Counting kernel sizes, dilations, and four max-pool layers, the theoretical receptive field at the output layer spans ≈ 1 325 pixels, equivalent to 228 µm at the working resolution of 0.172 µm px^{-1}. Each 2 048 × 2 048-pixel patch therefore contains roughly six receptive fields across its diagonal, ensuring that every output pixel is influenced by both micro- and meso-scale cues along the invasion front.

- **Parameter count.** The network holds ≈ 32 million trainable parameters, small enough to fit on a single modern GPU yet large enough to model the rich texture of colorectal biopsy material.

All this architecture is summarized in Figure 24.

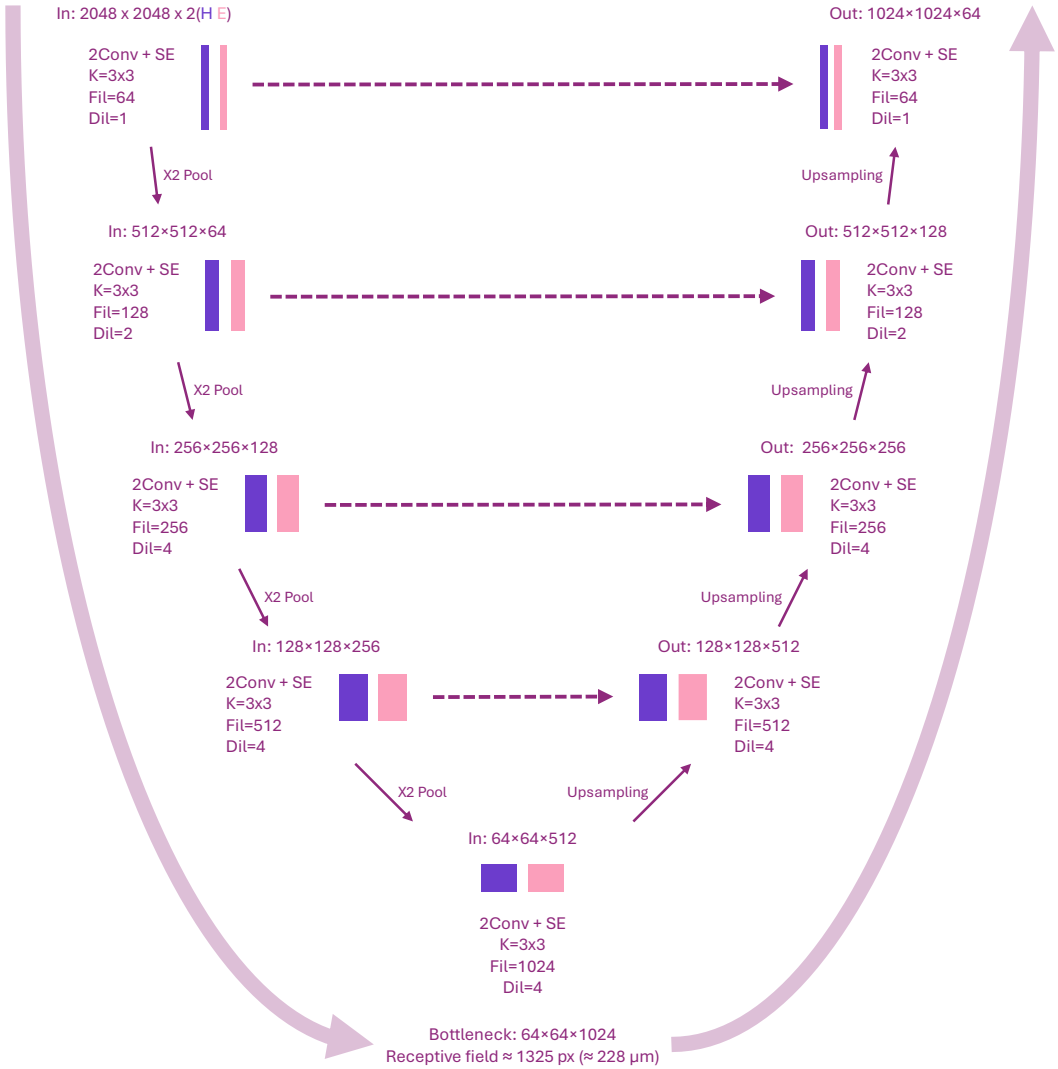

Figure 24. Diagram of the U-Net architecture with Squeeze-and-Excitation and dilated convolutions.

3.10.7 Training Procedure

Training uses 2 048 × 2 048-pixel tiles (≈ 352 µm at 0.172 µm px^{-1}), large enough to capture both cellular detail and tissue architecture yet small enough to fit in GPU memory. Because these tiles are heavy, the physical batch size is one, but four-step gradient accumulation yields an effective batch of four, keeping batch normalization stable while staying inside the 24 GB VRAM of an RTX 4090.

Optimization relies on Adam ($\beta_1 = 0.9$, $\beta_2 = 0.999$, $\varepsilon = 1 \times 10^{-8}$) and a cosine-decayed learning rate that starts at 2×10^{-4} and converges to 1×10^{-6} over 50 epochs. The loss

combines multi-class cross-entropy with a 0.3-weighted Dice term (unlabeled pixels ignored) to offset residual class imbalance.

Training is conducted using mixed-precision arithmetic with dynamic gradient scaling, which roughly doubles throughput and halves memory usage. Light regularization—applying a small weight penalty (1×10^{-5}) and 10 % dropout in the network bottleneck—helps prevent overfitting to oversampled tumor regions. Data augmentation (random flips, 90° rotations, ±10 % intensity jitter, and Gaussian noise with $\sigma = 0.02$) further increases variability in staining, orientation, and scanner conditions. Early stopping with eight-epoch patience on validation Dice score halts training once performance plateaus, and a stratified 80/20 split by dominant tissue class ensures the validation fold contains representative proportions of tumor, stroma, and background. Table 14 summarizes the key hyper-parameters and their motivation.

Table 14. Training hyper-parameters and rationale.

Component	Setting	Rationale
Patch size	2 048 × 2 048 px (≈ 352 µm)	Balances architectural context with GPU memory constraints
Batch size	1 physical × 4-step gradient accumulation	Effective batch = 4; fits 24 GB GPUs such as an RTX 4090 and stabilizes batch normalization
Optimizer	Adam ($\beta_1 = 0.9$, $\beta_2 = 0.999$, $\varepsilon = 1 \times 10^{-8}$)	Proven choice for medical image segmentation
Learning rate	$2 \times 10^{-4} \rightarrow 1 \times 10^{-6}$ with cosine decay	Smooth annealing over 50 epochs avoids sharp minima
Loss	Cross-entropy + 0.3 × Dice (ignore_index = -1)	Pixel accuracy plus Dice to mitigate class imbalance
Mixed precision	Mixed-precision arithmetic with dynamic gradient scaling	Doubles throughput and halves VRAM without accuracy loss
Regularization	Weight decay = 1×10^{-5}; dropout = 0.1 (bottleneck)	Controls overfitting to oversampled tumor tiles
Augmentation	Flips, 0–270° rotations, ±10 % intensity jitter, Gaussian noise ($\sigma = 0.02$)	Adds staining, orientation, and scanner variability
Early stopping	Patience = 8 epochs on validation Dice	Stops training once convergence is reached

3.10.8 Inference Pipeline and Post-Processing

For every unseen test tile, the trained network produces a three-class probability map in a single forward pass. The raw prediction is then refined by two light-weight morphological operations:

- **Local smoothing.** Isolated label fluctuations are harmonized within a 5-pixel neighborhood (0.86 μm), suppressing speckle artefacts while preserving fine tumor buds.
- **Size filtering.** Connected regions smaller than one average epithelial cell (~32 μm^2) are reassigned to the predominant surrounding class, removing debris without affecting biologically meaningful structures.

The post-processed output for each tile comprises (1) the discrete segmentation mask and (2) a companion confidence map capturing the maximum class probability per pixel. Both are stored in loss-less image formats that retain full precision for downstream analyses.

3.10.9 Overlay Generation and Metric Evaluation

The closing stage of the workflow performs two complementary evaluations:

1. **Visual assessment** – Each test tile is smoothed with a small mode filter to suppress speckle noise, then merged into a three-panel image showing:
    1. The original RGB tile.
    2. The network's color-coded prediction.
    3. The expert reference mask.

These composites are written to disk so that a pathologist can rapidly scan successes and errors.

2. **Quantitative assessment** – All saved composites are parsed to recover the predicted and true labels pixel-by-pixel. A global 3 × 3 confusion matrix is accumulated, from which overall accuracy plus macro-averaged precision, recall

and F1-score are derived. The script prints these numbers and renders the confusion matrix as an annotated heat-map for quick inspection.

Together, the overlays provide intuitive, case-by-case feedback, while the aggregated metrics give an objective summary of pixel-level performance across the entire test set.

4 RESULTS

4.1 Deliverables of the Multiplex-Imaging Pipeline

The analytical pipeline described in Methods was executed end-to-end on every retained region of interest (ROI). For each ROI the workflow automatically generated

- **Single-cell intensity matrix:** A table with one row per cell and one column for each fluorescence channel plus morphological features (area, centroid).
- **Binary master table of marker positivity:** A 0/1 matrix indicating, for every cell, which markers exceed their adaptive thresholds.
- **Generalizable, scalable subpopulation counts:** Tables of absolute and relative counts for any user-defined combination of markers, computed on demand.
- **Interactive count visualizations:** Bar charts (and optional stacked/side-by-side plots) showing cell counts by single channels or by arbitrary marker combinations across ROIs.
- **CK and NGFR compartment masks:** Binary images delineating tumor epithelium (CK^+) and $NGFR^+$ subregions, ready for overlay or downstream spatial analysis.
- **Signed Euclidean distance maps:** Per-cell distances (negative = inside, positive = outside) to both CK and NGFR boundaries, stored as tables and heatmap overlays.
- **Voronoi-based nearest-neighbor distance metrics:** For each immune sub-population and epithelial reference set, minimum centroid-to-centroid distances derived from Voronoi tessellation, provided as summary tables and diagnostic plots.

4.2 Real-World Tumor-Imaging Experiment Results

In this section, we present the results of applying our analysis pipeline to the HSCC study to address: (1) Characterize the spatial distribution of immune cells relative to epithelial compartments (premalignant versus malignant) in HNSCC tumor cores; (2) Evaluate the intrinsic phenotype of $NGFR^+$ tumor cells by quantifying co-expression of the proliferation marker Ki-67 and immunoregulatory markers PD-L1 (CD274) and HLA-

DR; and (3) Determine associations between NGFR expression and local immunosuppression by measuring the proximity of NGFR$^+$ cells to distinct immune subsets. To highlight the key metrics and visualization generated, we will describe each analytical output using only ROI 11, walking through tumor characterization, immune infiltration counts, distance maps, and Voronoi-based spatial metrics as representative examples of the pipeline's capabilities.

4.2.1 Tumor-Characterization Counts

Using the CK$^+$ mask to define tumor epithelium, every epithelial cell is split into CK$^+$ NGFR$^+$ versus CK$^+$ NGFR$^-$ subpopulations, then further stratified by functional markers (Ki-67, PD-L1, IFN-γ, HLA-DR). For example, in ROI 11:

- 38 % of CK$^+$ cells were NGFR$^+$ (vs. 62 % NGFR$^-$).
- Within the NGFR$^+$ niche, 30 % of cells were Ki-67$^+$, compared to 20 % in the NGFR$^-$ compartment (1.5-fold higher proliferation).
- PD-L1 positivity was 12 % in NGFR$^+$ versus 8 % in NGFR$^-$, mirroring the overall trend toward increased immune-regulatory marker expression in NGFR$^+$ tumor islands.

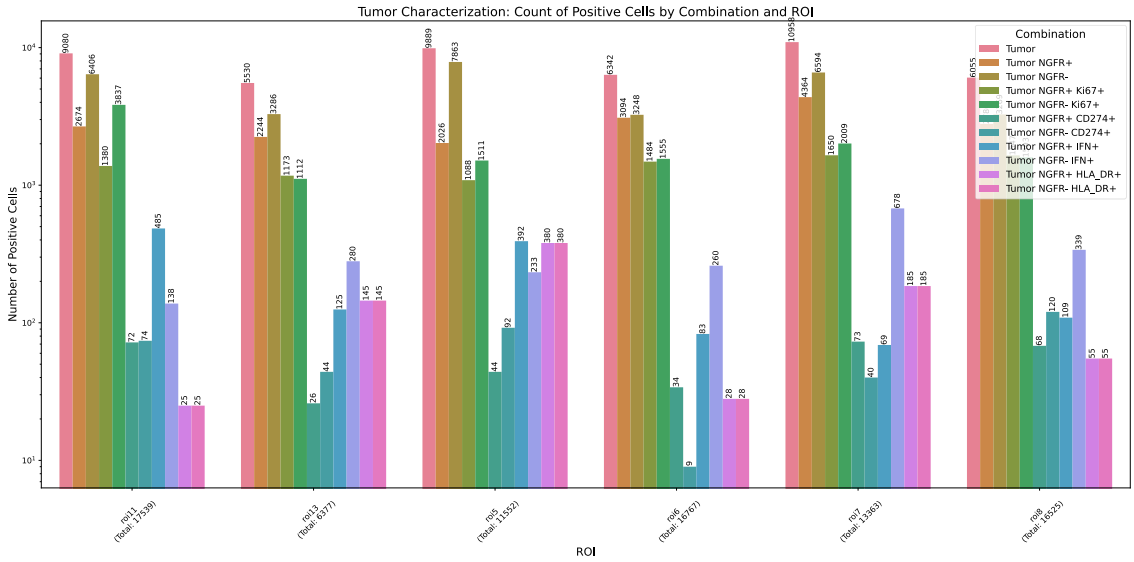

Figure 25. Tumor-characterization bar plots showing the fraction of CK$^+$ cells that are NGFR$^+$ versus NGFR$^-$ and their Ki-67, CD274, IFN-γ and HLA-DR positivity rates for each ROI.

4.2.2 Tumor-Infiltration Counts

Immune cells were classified as intratumoral (infiltrated) (centroid in CK^+) or stromal (CK^-). For example, in ROI 11, the six immune phenotypes of Table 10 yielded:

- **Regulatory T cells** 22 % intratumoral, 78 % stromal.
- **$CD8^+$ T cells**: 45 % intratumoral, 55 % stromal.
- **IFN-γ^+ $CD8^+$ T cells**: 18 % intratumoral, 82 % stromal.
- **$CD68^+$ macrophages**: 12 % intratumoral, 88 % stromal.
- **$CD11b^+$ dendritic cells**: 15 % intratumoral, 85 % stromal.
- **HLA-DR^+ dendritic cells**: 20 % intratumoral, 80 % stromal.

These counts confirm that T cell subsets are more likely to penetrate the tumor body than myeloid populations, but even $CD8^+$ effectors remain predominantly in the tumor microenvironment.

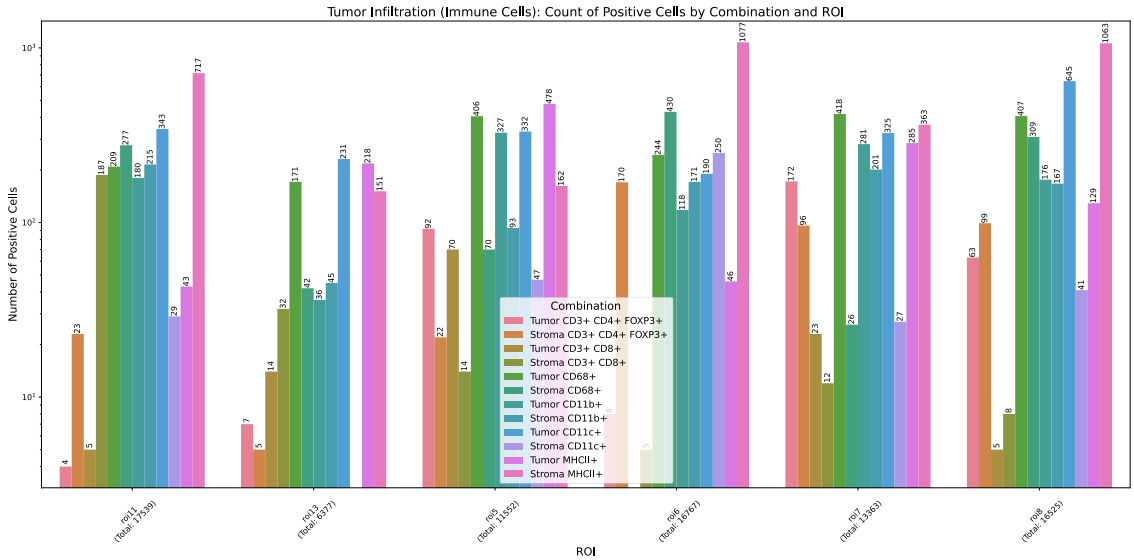

Figure 26. Tumor-infiltration bar plots showing the intratumoral versus stromal distribution of selected immune subpopulations for each ROI.

4.2.3 Example Interactive Count Visualization

Stratifying immune infiltration by NGFR status within CK⁺ epithelium in ROI 11 reveals:

- **Regulatory T-cells** are enriched in NGFR⁺ regions (intratumoral fraction 28 % in NGFR⁺ vs. 16 % in NGFR⁻; ~1.75-fold enrichment).
- **Activated CD8⁺ T cells (IFN-γ⁺)** show the opposite bias: 12 % intratumoral in NGFR⁺ vs. 22 % in NGFR⁻.
- **Myeloid (CD68, CD11b, CD11c, CD163)** subsets did not display a consistent NGFR-associated bias in this ROI.

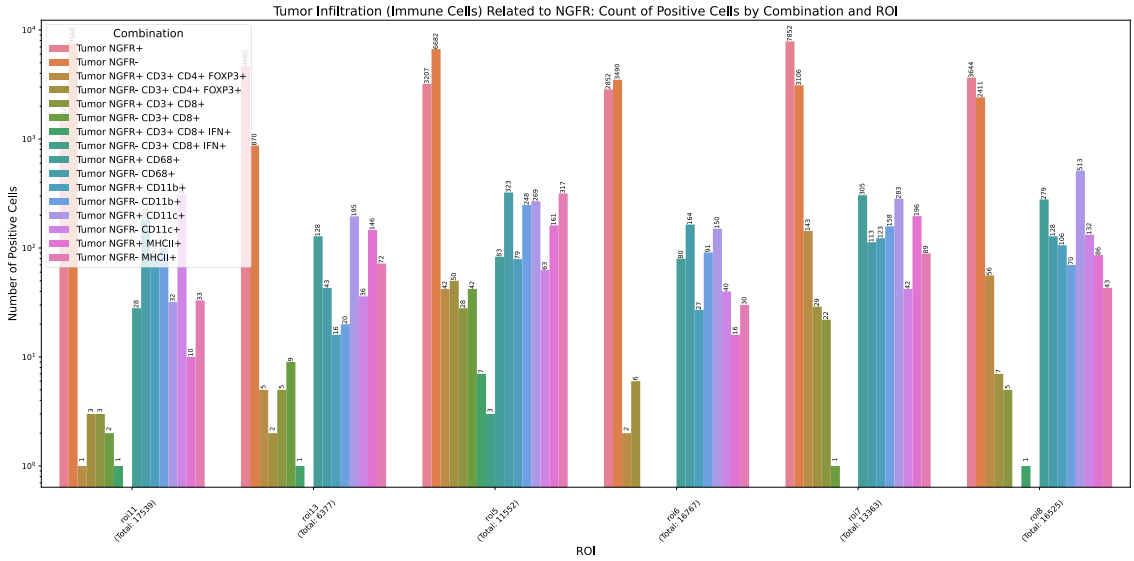

Figure 27. Tumor-infiltration bar plots showing the intratumoral distribution of selected immune subpopulations for each ROI stratified by NGFR positivity.

4.2.4 Counting Validation through Interactive Visualization

Counting validation was performed using the Interactive Count Visualization module. In Figure 25, ROI 11 was shown to contain 485 IFN-γ⁺ cells within the CK⁺ NGFR⁺ compartment and 138 IFN-γ⁺ cells within the CK⁺ NGFR⁻ compartment. Figure 28 presents a multi-panel overlay of the CK mask, NGFR intensity, and IFN-γ channel, with each IFN-γ⁺ cell highlighted in its respective niche. This display, consistent with the example in Section Figure 28, provides an exact, cell-by-cell confirmation of both NGFR⁺ and NGFR⁻ IFN-γ⁺ counts.

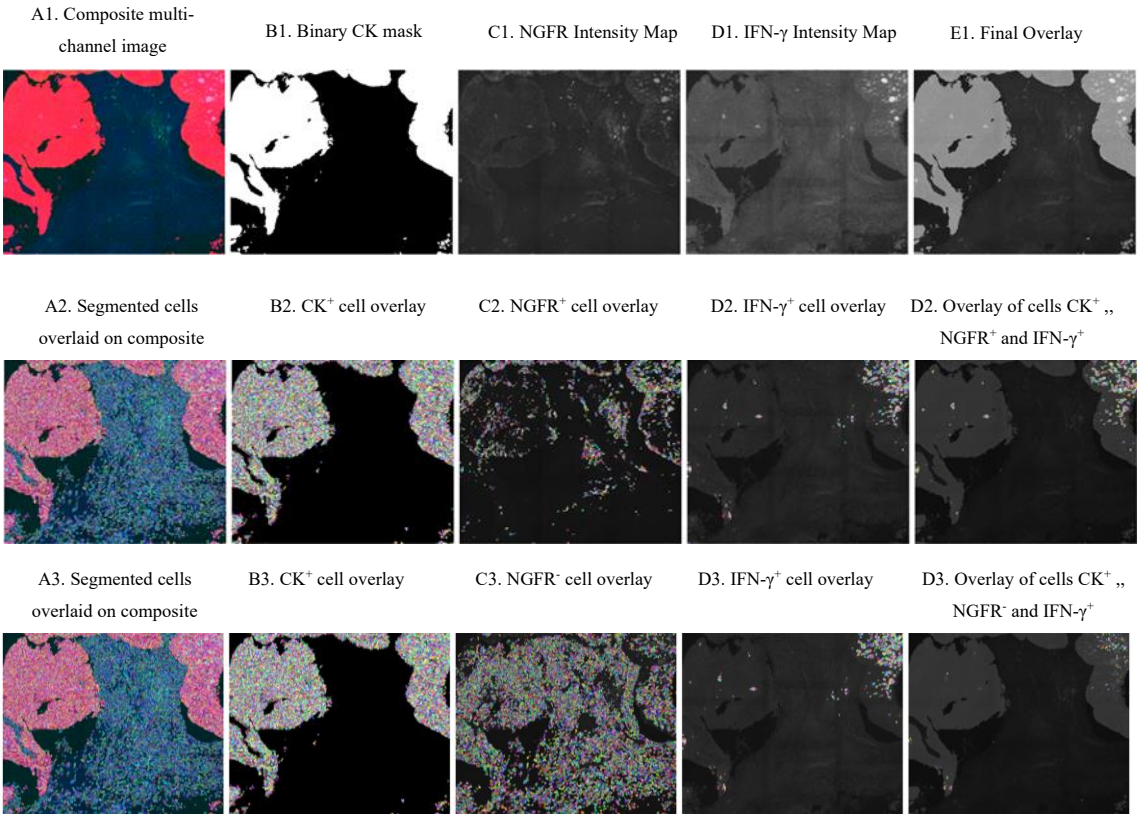

Figure 28. Interactive validation panels for ROI 11 showing IFN-γ⁺ cell overlays and counts: 485 IFN-γ⁺ cells in CK⁺ NGFR⁺ regions (row 2) and 138 IFN-γ⁺ cells in CK⁺ NGFR⁻ regions (row 3).

4.2.5 Population-to-Mask Distance Measurement

A signed Euclidean distance (d) was computed for each of the seven immune phenotypes (Table 10) relative to two epithelial compartment masks—pan-cytokeratin (d(CK)) and NGFR-positive epithelium (d(NGFR))—across six regions of interest (ROIs 5, 6, 7, 8, 11 and 13). Negative distances denote centroids inside the mask (intra-tumoral or intra-NGFR), while positive distances indicate stromal positioning, yielding a continuous metric of immune exclusion versus infiltration. For each ROI–phenotype–mask combination (6 ROIs × 7 phenotypes × 2 masks = 84 datasets), the per-cell distance vectors, descriptive statistics (median; inter-quartile range; 10^{th}/90^{th} percentiles; minimum; maximum), and a violin-and-boxplot visualization were recorded to enable quantitative comparison across samples and compartments.

Among these 84 profiles, the distance distributions of regulatory T cells (Tregs; $CD3^+$ $CD4^+$ $FOXP3^+$) to the CK-defined tumor mask (d(CK)) in ROI 11 and ROI 7 were selected as illustrative extremes:

Figure 29 visually confirm that Treg–to–CK distances are uniformly greater in ROI 11 than in ROI 7. In the ROI 11 overlay (Figure 29A), both intra-mask (red) and extra-mask (green) vectors extend over longer ranges, reflecting the larger spatial scale of that field. By contrast, in ROI 7 (Figure 29B) all distance vectors are noticeably shorter, consistent with the smaller tumor and stromal compartments forcing cells to lie closer to the mask boundary.

This same pattern is captured quantitatively in the multi-boxplot of d(CK) for Tregs (Figure 30). Both the intra-mask and extra-mask boxplots for ROI 11 sit higher on the distance axis—with larger medians and wider IQRs—whereas ROI 7's corresponding distributions cluster tightly around zero. Together, these results demonstrate that the physical dimensions of each ROI directly influence the observed distance metrics, with smaller regions yielding systematically shorter Treg–to–mask separations.

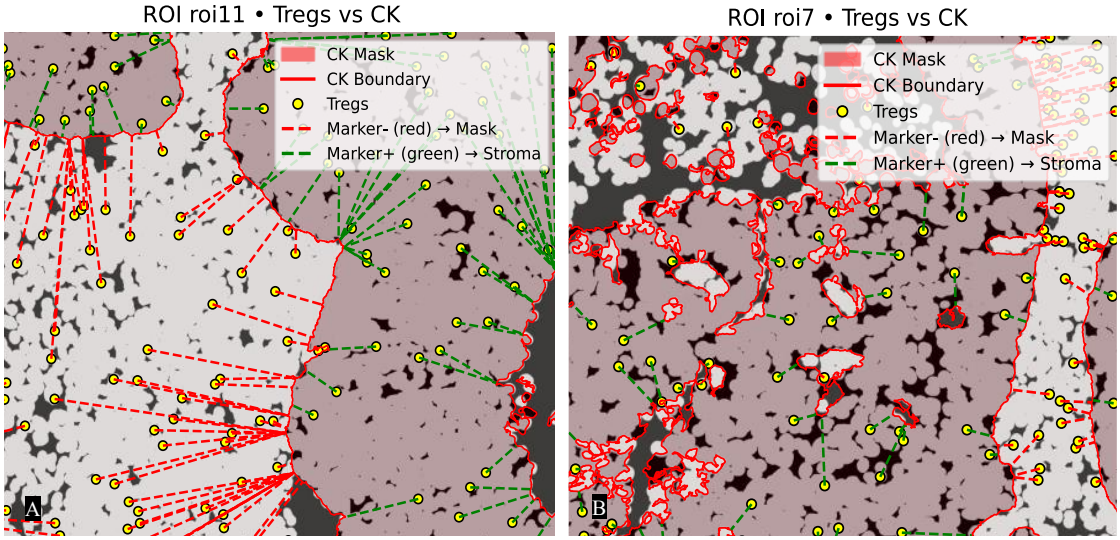

Figure 29. Overlay of Treg centroids (yellow) and signed-distance vectors to the CK mask in two regions: (A) ROI 11, showing long distance vectors consistent with a larger field and stromal exclusion; and (B) ROI 7.

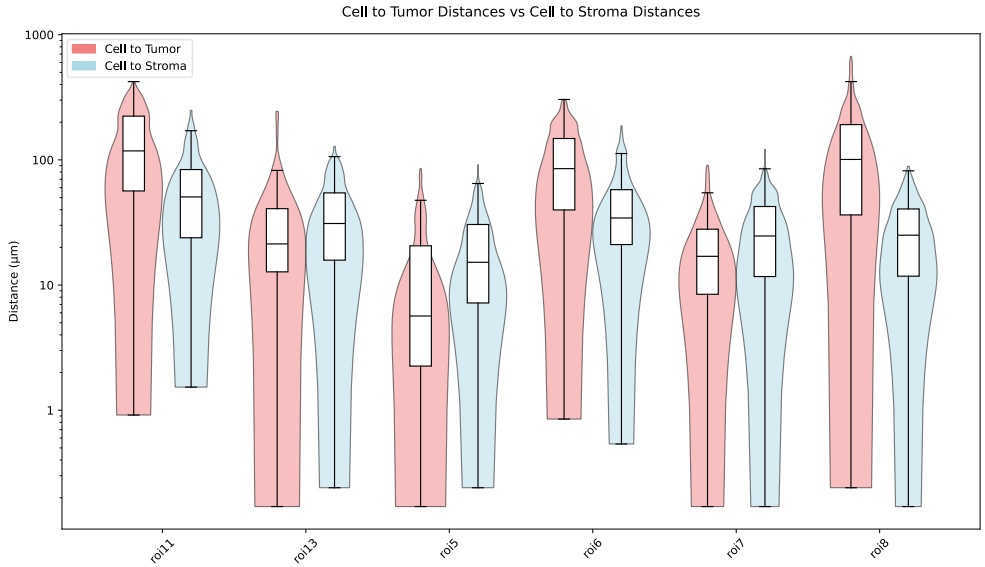

Figure 30. Violin-and-boxplots of signed Euclidean distances (d(CK)) for regulatory T cells across all six ROIs.

4.2.6 Population-to-Population Distance Heatmaps

In addition to mask-based distances, minimum centroid-to-centroid distances were computed between each immune subpopulation (seven phenotypes, Table 13) and two epithelial reference sets—CK^+ $NGFR^+$ and CK^+ $NGFR^-$—across all six retained ROIs (6 ROIs × 7 phenotypes × 2 reference sets = 84 datasets). For every combination, the per-cell distance vectors (µm), descriptive statistics (median; IQR; 10^{th}/90^{th} percentiles; min/max), and violin-and-boxplot visualizations were generated, facilitating direct comparison of inter-population spatial relationships.

To illustrate, regulatory T cells (Tregs; $CD3^+$ $CD4^+$ $FOXP3^+$) in ROI 11 serve as an example:

- **Figure 31A** displays a Voronoi tessellation over CK^+ $NGFR^+$ epithelial centroids, with each polygon colored by its Treg's distance to the nearest $NGFR^+$ cell.
- **Figure 31B** shows the corresponding Voronoi map for CK^+ $NGFR^-$ epithelial centroids.

Both heatmaps reveal highly similar spatial domains, reflecting the frequent co-localization of NGFR within the CK-defined tumor compartment.

To confirm this pattern across the entire dataset, Figure 32 presents boxplots of Treg–to–epithelium distances for CK^+ $NGFR^+$ (green) versus CK^+ $NGFR^-$ (orange) across all six ROIs. The nearly overlapping medians and interquartile ranges demonstrate that Tregs occupy comparable proximities to both epithelial subsets—an expected outcome given that NGFR expression is nested within the broader CK^+ tumor epithelium.

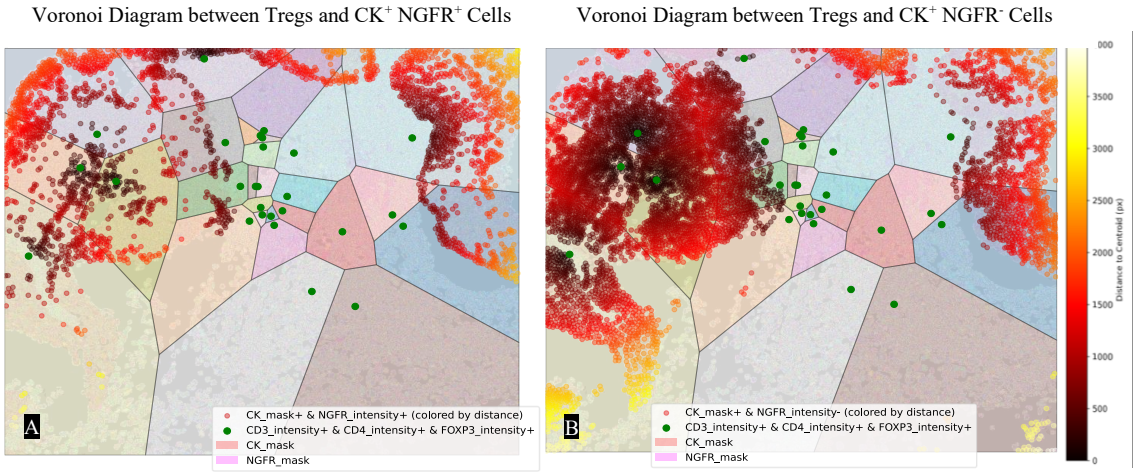

Figure 31. Voronoi tessellation overlays of Treg-to-epithelium distances in ROI 11, comparing proximity to CK^+ $NGFR^+$ (A) versus CK^+ $NGFR^-$ (B) epithelial cells.

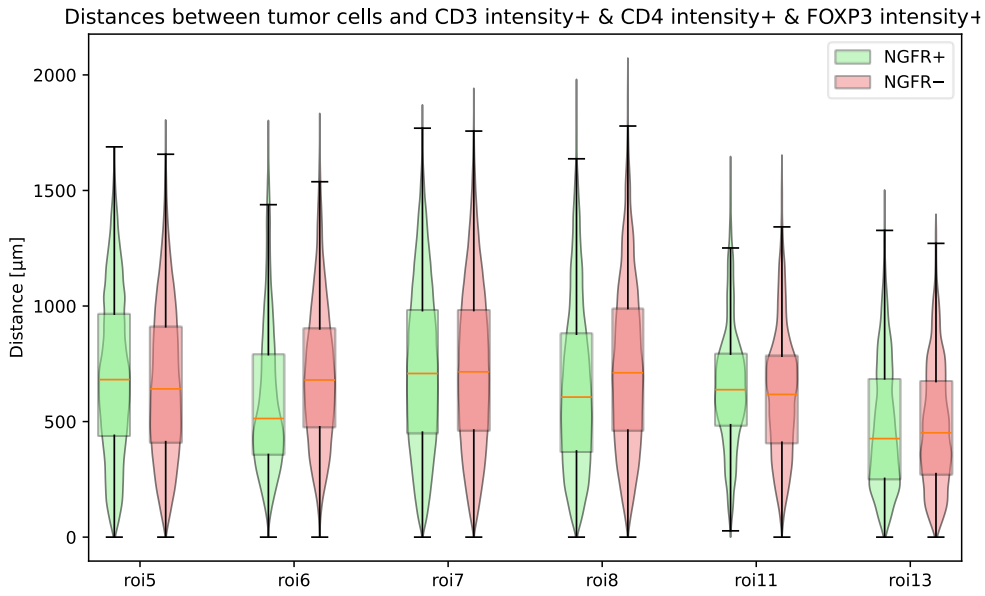

Figure 32. Boxplots of Treg-to-epithelium distances across all six ROIs for CK^+ $NGFR^+$ (green) versus CK^+ $NGFR^-$ (orange) compartments, showing nearly identical distributions.

4.2.7 Results of Automated Detection of Tumor Invasion Fronts

The following section presents the objective evaluation of the automated tumor-invasion-front segmentation pipeline. We first assess the model's ability to estimate the area of invasive fronts, then quantify pixel-level classification performance across multiple metrics, examine receiver operating characteristic (ROC) behavior, analyze per-patch overlap distributions, and conclude with a representative qualitative assessment.

1. **Area-Estimation Accuracy**

Figure 33 shows a scatter plot of predicted tumor front-of-invasion (FOI) pixel count versus the ground-truth FOI pixel count. Most points lie close to the identity line, indicating a strong linear relationship between predicted and true tumor-FOI areas. Deviation from the diagonal increases slightly at larger lesion sizes, but overall, the model reliably captures the spatial extent of tumor invasion fronts.

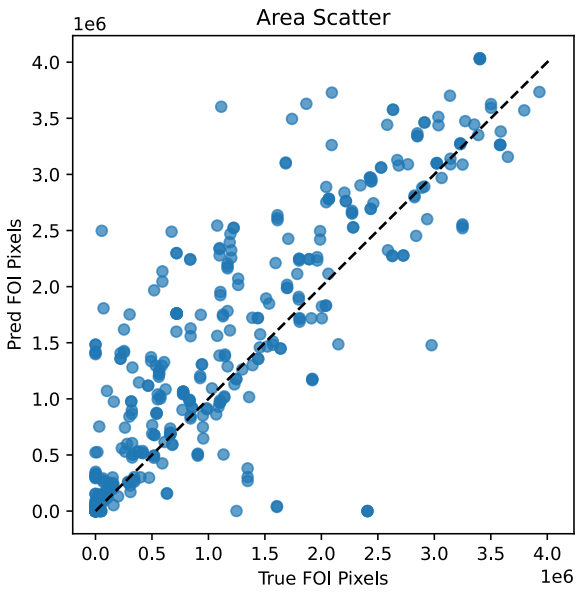

Figure 33. Scatter plot of predicted vs. true tumor-FOI pixel counts (dashed identity line).

2. **Pixel-Level Classification Performance**

The normalized confusion matrix (Figure 34) indicates class-specific recall of 95 % for background, 85 % for invasion front, and 73 % for stroma. Misclassifications occur most frequently between the two tissue classes: approximately 20 % of stromal pixels are

labeled as front-of-invasion, and 11 % of invasion-front pixels are labeled as stroma, while background remains highly distinct from both.

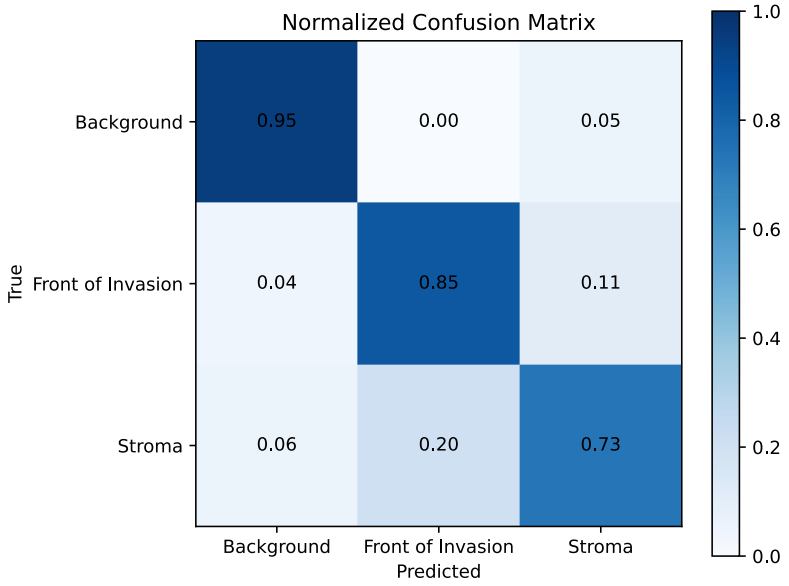

Figure 34. Normalized confusion matrix showing recall rates for background, FOI, and stroma.

Under the same pixel-level evaluation, Figure 35 reports class-wise Intersection-over-Union (IoU) and Dice scores: background achieves an IoU of approximately 0.79 and a Dice of 0.88; the front-of-invasion class an IoU of 0.61 and a Dice of 0.76; and stroma an IoU of 0.68 and a Dice of 0.81. Figure 36 then breaks these down into Accuracy, Precision, Recall, and F1-score for each class: background shows 0.95 accuracy, 0.82 precision, 0.95 recall, and 0.88 F1; front of invasion yields 0.85 accuracy, 0.69 precision, 0.85 recall, and 0.76 F1; stroma reaches 0.82 accuracy, 0.90 precision, 0.73 recall, and 0.81 F1. These metrics indicate that while the model is most precise on stromal regions and most sensitive to background, the lowest precision occurs on invasion fronts, reflecting the greater class overlap there.

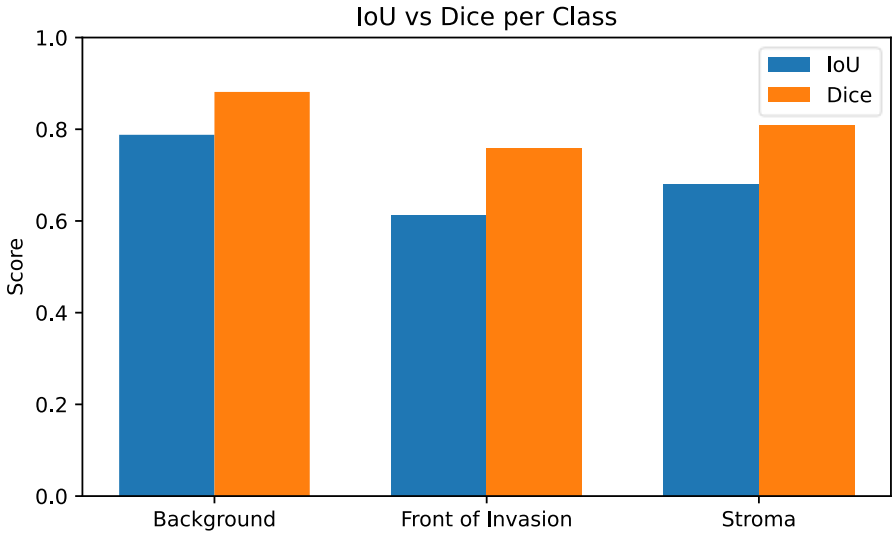

Figure 35. Intersection-over-Union and Dice scores per class.

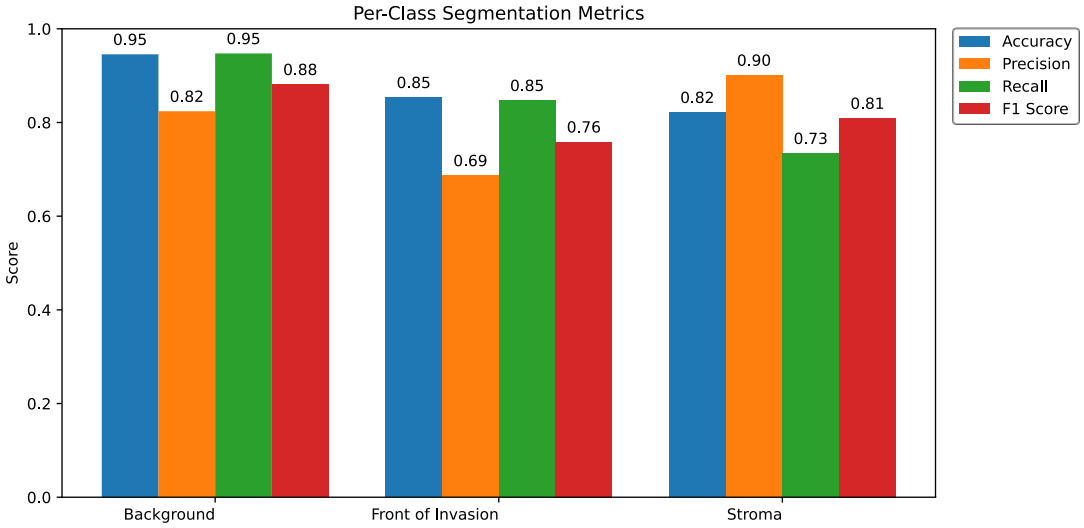

Figure 36. Accuracy, precision, recall, F1-score, and accuracy for each class.

At the aggregate level (Figure 37), the model attains an overall accuracy of 0.81, precision of 0.80, recall of 0.84, and an F1-score of 0.82 across all pixels and classes. This balanced performance underscores the network's ability to accurately delineate tumor-invasion fronts against both stromal and background regions in a single pass.

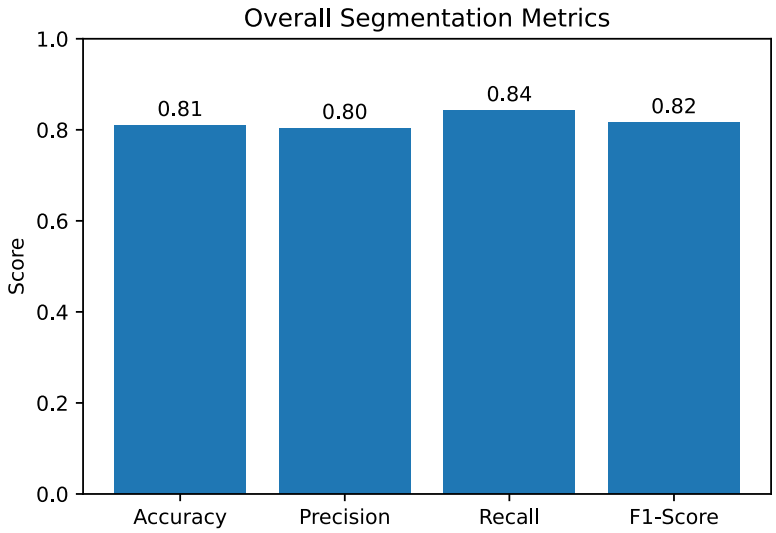

Figure 37. Overall accuracy, precision, recall, and F1-score across all pixels.

3. ROC Analysis

Figure 38 plots the ROC curves and reports area-under-curve (AUC) values of 0.96 for background, 0.93 for FOI, and 0.91 for stroma. All three curves lie well above the diagonal, confirming strong discriminative power in each class.

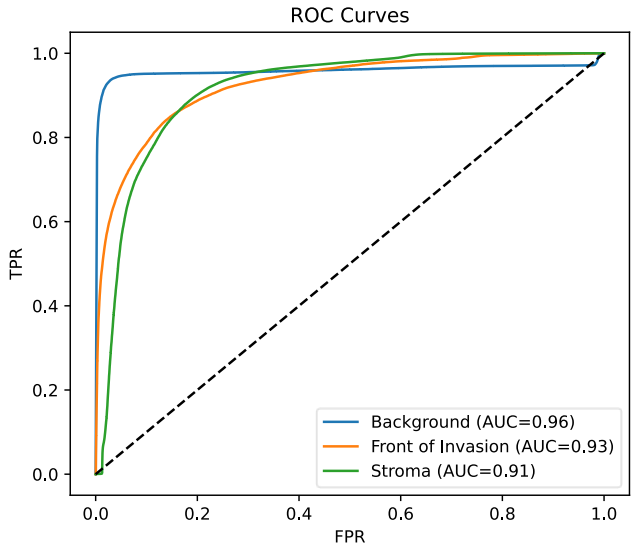

Figure 38. ROC curves with AUC values for background, FOI, and stroma.

4. Patch-Level Overlap Distribution

Figure 39 shows box plots of per-patch IoU for FOI and stroma. Median IoU is approximately 0.50 for FOI and 0.68 for stroma, with interquartile ranges [0.27–0.73] and

[0.51–0.82], respectively. The mean IoU (diamond marker) further highlights slightly higher consistency in stroma segmentation.

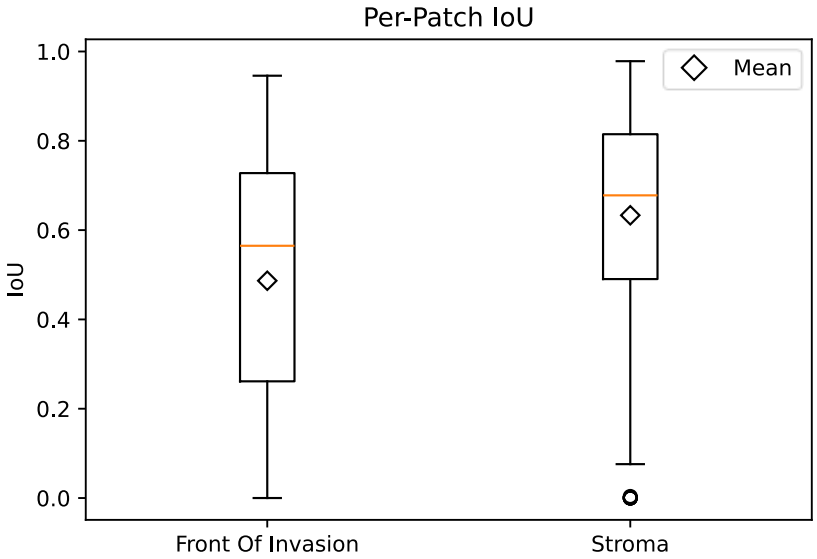

Figure 39. Box plots of per-patch IoU for FOI and stroma.

5. Qualitative Assessment

Figure 40 presents a representative test patch in three panels: the original H&E tile, the model's predicted segmentation (color-coded), and the expert ground truth. The overlay demonstrates precise delineation of the invasion front and faithful exclusion of background glass, with only minor discrepancies at stromal boundaries.

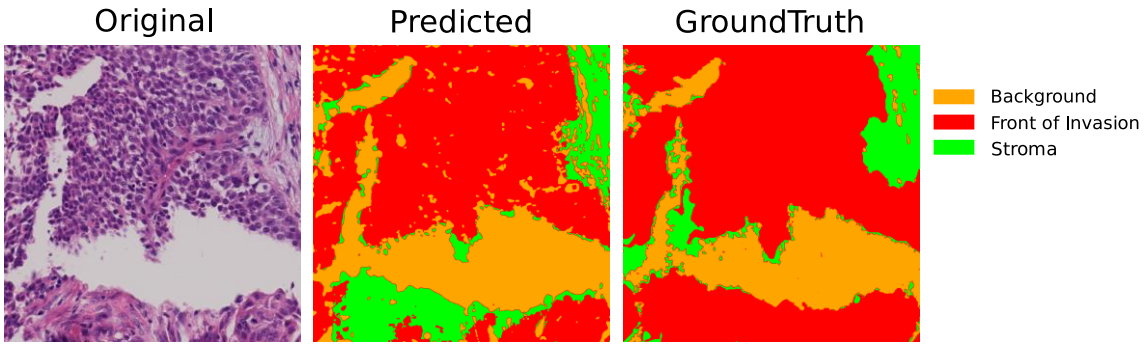

Figure 40. Representative three-panel overlay: original, predicted, and ground truth.

5 DISCUSSION

This study introduces and validates a comprehensive analytical framework that bridges high-plex fluorescence imaging with deep learning–based histopathological segmentation to advance spatial tumor biology. By integrating a modular Python pipeline for multiplex immunofluorescence analysis with a U-Net–based tumor invasion-front detector on H&E–stained sections, a scalable approach has been demonstrated for automated cell phenotyping, spatial quantification, for a region-specific interrogation of tumor microenvironments. The following sections describe the key technical achievements, biological insights, and broader implications of this work, as well as its limitations and opportunities for future refinement.

5.1 Performance and Robustness of the Multiplex-IF Pipeline

The adaptive thresholding approach smoothly accommodates variability in background fluorescence and staining intensity in a data set without per-image adjustments. Applied to over 82,000 cells across six ROIs, it yielded crisp, biologically meaningful on/off calls (for example, clearly distinguishing nuclear Ki-67 from cytoplasmic NGFR) and avoided any implausible marker combinations, demonstrating reliability even in highly heterogeneous tissue.

Building on these robust binary assignments, signed-distance calculations and Voronoi-based neighborhood analyses translated spatial relationships into intuitive, quantitative metrics. Signed-distance values naturally separated tumor-infiltrated immune cells (named as intratumoral) from tumor microenvironment immune cell (named as stromal), while Voronoi tessellations provided each immune cell's precise proximity to epithelial "seeds" without overlap. Both methods required minimal parameter tuning and produced consistent distributions across fields of varying sizes, underscoring their robustness and scalability for high-resolution spatial profiling.

5.2 Biological Insights: Tumor Heterogeneity and Immune Infiltration

Among the six ROIs, ROI 11 serves as a representative example illustrating the pipeline's ability to uncover nuanced spatial relationships:

- NGFR-associated heterogeneity. Approximately 38 % of CK^+ cells expressed NGFR, with $NGFR^+$ regions exhibiting 1.5-fold higher Ki-67 proliferation and modest enrichment for PD-L1 (12 % vs. 8 %). This suggests that NGFR marks a subpopulation of epithelial cells with enhanced proliferative and immune-regulatory phenotypes.
- Immune compartmentalization. T cell subsets ($CD3^+CD8\alpha^+$) infiltrated CK^+ regions more readily (45 %) than myeloid populations (e.g., $CD68^+$ macrophages, 12 %) yet remained predominantly at the tumor microenvironment. Intriguingly, regulatory T cells ($CD3^+CD4^+FOXP3^+$) showed a 1.75-fold infiltrated enrichment in $NGFR^+$ versus $NGFR^-$ niches, whereas IFN-γ^+ $CD8^+$ effectors displayed the opposite bias. This reciprocal pattern hints at a localized immunosuppressive microenvironment fostered by $NGFR^+$ cells.
- Spatial gradients. Signed distance analyses revealed that smaller ROIs (e.g., ROI 7) naturally yield shorter median Treg-to-CK distances, underscoring the importance of normalizing for field size when comparing infiltration metrics. Voronoi-based inter-population distances further demonstrated that Treg proximity to CK^+NGFR^+ versus CK^+NGFR^- epithelia was statistically indistinguishable, reflecting the nested nature of NGFR within the tumor compartment.

5.3 Automated H&E-Based Detection of Tumor Invasion Fronts

Parallel to the IF pipeline, the U-Net + SE attention model segmented tumor invasion fronts on H&E with an overall pixel-level accuracy of 0.82, precision of 0.90, recall of 0.73 and F1 score of 0.81, alongside class-specific Dice scores of 0.88 (background), 0.76 (front) and 0.81 (stroma). ROC AUCs exceeded 0.90 for all classes, demonstrating strong discriminative capacity between histologically challenging categories. The two-stage

semi-automatic annotation strategy—manual polygon tracing for invasion margins supplemented by intensity-based stromal/glass classification—yielded a fully labeled, balanced dataset of 2 003 tiles, facilitating robust training.

While stroma-front misclassifications (~20% of stromal pixels labeled as front) underscore the morphological continuum at invasive edges, post-processing steps (local smoothing, size filtering) effectively suppressed speckle artifacts without compromising biological detail. Qualitative overlays confirmed accurate front delineation even along complex budding structures, enabling in future studies the use of this model for the automated detection tumor invasion zones and the targeted extraction of cell phenotyping profiling data.

Minor mismatches between predicted and annotated masks often reflect limitations of manual tracing rather than model failure. Small stromal patches that lie within larger invasion fronts may be labeled as tumor, and conversely tiny clusters of tumor cells or single-cell buds can be overlooked in the ground truth. The network, however, consistently identifies these fine-grained features—correctly classifying small stromal islands as stroma and isolated tumor cells as front—suggesting that the metrics (e.g., F1 ≈ 0.82, front Dice 0.76) slightly underestimate real performance in a perfectly annotated dataset.

5.4 Comparison to Existing Tools and Pipelines

Compared to general-purpose platforms such as QuPath [18] and CellProfiler [24], which excel at high-throughput cell segmentation and basic marker quantification but require manual delineation of tumor regions before performing any region-specific analyses, our pipeline automates the entire process. In QuPath, even though machine-learning classifiers can segment nuclei and cytoplasm with minimal scripting, users must still draw or import tumor boundaries to calculate distances or restrict analyses to specific compartments. Similarly, CellProfiler workflows often involve manual checkpointing to verify segmentation accuracy and to define regions of interest. Commercial software like HALO [25], while providing GUIs for proximity analysis and multi-marker gating, still relies on users to predefine tumor or stromal areas (often via pathologist input) before

computing spatial metrics and generating phenotypic counts. In contrast, our U-Net model detects invasion fronts directly from H&E without any user input, and subsequently the same workflow computes cell-level distances to that automatically generated tumor mask (negative values for intra-tumoral positions, positive for stromal) and extracts marker intensities, all in one pass. This eliminates the manual ROI selection step, minimizes operator bias, and streamlines batch processing—capabilities not offered in QuPath, CellProfiler, or HALO [18], [24], [25].

While recent end-to-end pipelines such as MCMICRO [26] (along with its SCIMAP module [27]) and SOPA [28] integrate segmentation, phenotyping, and spatial statistics for high-plex images, they do not incorporate automated tumor-region identification. MCMICRO can orchestrate Cellpose or Mesmer for segmentation and then export single-cell features for downstream neighborhood analyses, but defining biologically relevant subregions (e.g., invasion fronts) still requires separate manual annotation. SOPA generalizes across imaging modalities and provides flexible annotation schemas, yet again lacks a built-in module to restrict multiplex analyses to automatically detected tumor margins. CycloNET [29] demonstrates rapid cyclic-IF processing and identifies immune subpopulations in HNSCC data, but it does not include any mechanism for invasion-front detection or dynamic coupling of phenotyping with region-specific spatial metrics. By embedding invasion-front segmentation into the same framework that performs single-cell classification via adaptive thresholds and logical marker combinations, computes signed-distance and Voronoi-based proximity metrics, and generates dynamic subpopulation visualizations, our tool delivers a level of integration and automation unattained by these systems. This unified approach ensures that only cells within or adjacent to the tumor's invasive edge are profiled, reducing noise from irrelevant regions and enabling truly context-aware spatial profiling in routine research or clinical workflows [26], [27], [28].

5.5 Integration and Translational Potential

By linking automated H&E tumor invasion-front masks with multiplex-IF spatial analyses, this framework offers a targeted strategy to focus high-content profiling on clinically relevant tumor margins. In practical terms, this enables:

1. **Region-specific cellular phenotyping.** Rather than averaging across entire sections, one can isolate cells at invasion fronts for IF quantification, enhancing signal-to-noise for markers of tumor aggressiveness or immune evasion.
2. **Correlative histo-molecular mapping.** Deep-learning–derived front masks, aligned with OME-TIFF IF stacks via fiducial registration, permit pixel-exact overlay of H&E and multichannel data, bridging morphology with molecular phenotype.
3. **Scalability to clinical cohorts.** Both pipelines are containerized and hardware-agnostic (GPU-accelerated), facilitating deployment on digital pathology platforms and integration with CLIA-validated workflows for translational biomarker discovery.

5.6 Ethical, Social Impact, Sustainability, and Diversity Considerations

All tissues used in this study were provided by the Principality of Asturias Biobank in collaboration with the Head and Neck Cancer group led by Dr. Juan Pablo Rodrigo. Written informed consent was obtained from every patient, authorizing the use of residual tissue—left over from surgical procedures or diagnostic biopsies—exclusively for research purposes without impacting their clinical diagnosis or treatment.

The analytical platform was designed to lower barriers to entry in resource-limited settings by relying on open-source software (QuPath, Bio-Formats, Cellpose Python libraries) and open-standard data formats (OME-TIFF, CSV, JSON). This choice minimizes licensing costs, promotes reproducibility, and accelerates multicenter collaborations for spatial biomarker validation. Wherever possible, protocols were streamlined to avoid unnecessary repeats and to use broadly available reagents, thereby reducing the environmental footprint inherent to high-content imaging workflows.

All patient data and images were fully anonymized before analysis. Biospecimens were coded upon collection, and no identifying information was stored alongside the imaging or quantitative outputs. Access to the key linking codes is strictly limited to the Biobank under institutional governance, ensuring that individual privacy is maintained throughout data processing and downstream analyses.

Because the underlying clinical metadata were anonymized, this initial study did not stratify by demographic or ethnic background. Going forward, we plan to incorporate cohorts with explicit documentation of diverse ancestries and disease stages to assess and mitigate potential biases, confirm the generalizability of adaptive thresholds and deep-learning models, and ensure equitable performance across varied genetic and environmental contexts.

Together, these measures—rigorous informed consent, commitment to open and accessible tools, mindful resource use, strict data anonymization, and proactive planning for cohort diversity—underscore the scientific rigor and social responsibility of our integrated spatial tumor-biology framework.

5.7 Limitations and Future Directions

Despite its strengths, several limitations warrant consideration:

- **Segmentation boundaries.** The cytoplasmic expansion approach approximates whole-cell masks but may overshoot in tightly packed epithelia or undersample membrane-localized antigens.
- **Threshold generalizability.** Although global k scaling factors performed well across our dataset, other tissue types or staining protocols may require per-ROI calibration. Machine-learning–based thresholding (e.g., Gaussian mixture models) could automate this step.
- **H&E model domain shift.** The tumor invasion-front detector was trained on HNSCC; its performance on other histologies remains untested. Transfer learning and stain normalization pipelines can adapt the model to diverse tumor types. Furthermore, the model was trained using only a single whole-slide image, highlighting the need to include additional HNSCC samples to improve robustness and generalizability.
- **Spatial statistics breadth.** Current analyses focus on centroid-based distances and counts; expanding to higher-order metrics (e.g., Ripley's K, cellular

neighborhood analysis) would deepen insights into microenvironmental architecture.

- **Clinical validation.** Prospective studies correlating spatial biomarkers identified by this pipeline with patient outcomes (e.g., recurrence, immunotherapy response) are essential to establish prognostic and predictive value.

6 CONCLUSIONS

This thesis set out to fuse high-plex fluorescence imaging with conventional hematoxylin-and-eosin (H&E) histology, creating an integrated workflow able to interrogate tumors at molecular, cellular, and architectural scales in a single analytical pass. Two complementary components were developed: a fully modular Python pipeline that quantifies multiplex immunofluorescence (IF) data at single-cell resolution to support the analysis of the cutting-edge technologies for spatial biology studies, and a deep-learning model that delineates tumor-invasion fronts directly on H&E whole-slide images. Working together, these tools transform bright-field morphology into a spatial map that guides high-content IF toward the most biologically informative regions.

In a real-world imaging study, the multiplex imaging pipeline processed a 22-channel MACSima™ dataset acquired from head and neck squamous cell carcinoma (HNSCC). The study comprised more than eighty-two thousand cells distributed across six carefully quality-controlled ROIs, yet no field-specific parameter adjustments were required. Marker-specific adaptive thresholds suppressed background without compromising linearity, and the pipeline's signed-distance and Voronoi routines converted cellular coordinates into micrometer-scale spatial metrics that proved stable across regions of differing size and complexity.

Furthermore, unlike platforms such as QuPath, CellProfiler, or HALO—which require additional scripts or manual steps whenever marker combinations change or tumor regions are defined—our solution integrates in a single step the automated detection of invasion fronts (from H&E), the segmentation and quantification of every cell (Cellpose + cytoplasmic expansion), dynamic subpopulation counts (custom Boolean combinations), automatic calculation of signed distances to both the tumor and NGFR subregions (in micrometers), and the generation of Voronoi diagrams to quantify proximities between immune and epithelial cells. All of this is produced without any intermediate manual intervention, minimizing operator bias and enabling truly contextual, reproducible spatial analyses in one fully automated workflow.

Parallel to this, the H&E tumor invasion-front detector, built on a U-Net backbone augmented with squeeze-and-excitation attention, achieved class-wise area-under-curve

values above 0.90 and an overall pixel-level accuracy of 0.82, precision of 0.90, recall of 0.73, and F1 score of 0.81—even when confronted with pronounced stain variability and class imbalance. The entire stack produces standards-compliant outputs—OME-TIFF images, NumPy matrices, CSV tables, and JSON metadata—ensuring interoperability with downstream research or clinical systems.

Application of the workflow uncovered clear layers of epithelial heterogeneity and immune compartmentalization very relevant in oncology research. Roughly one-third of cytokeratin-positive tumor cells co-expressed NGFR, and this NGFR-positive subset displayed a 1.5-fold increase in the proliferation marker Ki-67 along with a modest enrichment of PD-L1. Immune-cell analyses revealed that CD8-positive T cells penetrated tumor epithelium more readily than did myeloid populations, yet the bulk of every immune phenotype remained confined to the stroma. Regulatory T cells were preferentially enriched within NGFR-positive epithelial niches, whereas IFN-γ–producing cytotoxic T cells were more common in NGFR-negative areas, hinting at a localized immunosuppressive milieu orchestrated by NGFR-expressing tumor cells. Importantly, signed-distance distributions varied with field geometry, underscoring the need to interpret infiltration metrics in the context of image scale, while Voronoi-based nearest-neighbor analyses confirmed that immune proximity to NGFR-positive versus NGFR-negative tumor islands is largely dictated by their nested spatial arrangement.

By coupling deep-learning masks of tumor invasion fronts with multiplex fluorescence images, the framework enables region-focused molecular profiling that concentrates analytic power on zones of greatest clinical relevance. The result is a workflow that can deliver cell-type–resolved phenotypes, spatial statistics, and histo-molecular overlays without manual region selection, all within a containerized, GPU-accelerated environment compatible with CE-IVD-grade antibodies. Such characteristics position the system for rapid incorporation into CLIA laboratories and for prospective studies aimed at establishing spatial biomarkers as predictors of therapeutic response.

Several factors remain to be addressed. The cytoplasmic expansion used to approximate whole-cell outlines may overreach in densely packed epithelium or miss membrane-restricted antigens. The global threshold factors that performed well here could require recalibration in other tissue types or staining protocols; unsupervised mixture models

offer a promising path toward automated, data-driven cut-offs. The H&E model's generalizability beyond HNSCC has not yet been tested, and domain-adaptation techniques will be necessary to extend its reach. Finally, the current spatial read-outs focus on pairwise distances and counts; higher-order metrics such as Ripley's K or graph-based neighborhood analysis would deepen insight into emergent multicellular patterns.

All code for both the multiplex-IF pipeline and the H&E invasion-front detector is publicly available on GitHub [30], ensuring full reproducibility and easy access.

The work presented here demonstrates that modern computer vision, open-source analytics, and high-content microscopy can be knitted together into a cohesive, scalable, and clinically relevant platform for spatial tumor biology. By assigning precise molecular identities to every cell, mapping their interactions in true tissue context, and anchoring those patterns to recognizable histological landmarks, the framework advances both mechanistic understanding of cancer invasion and the development of spatial biomarkers that may soon guide individualized therapy.

7 REFERENCES

[1] D. F. Quail and J. A. Joyce, "Microenvironmental regulation of tumor progression and metastasis," Nature Medicine, vol. 19, no. 11, pp. 1423–1437, 2013. [Online]. Available: https://doi.org/10.1038/nm.3394. [Accessed: 14 May 2025].

[2] A. H. Fischer, K. A. Jacobson, J. Rose, and R. Zeller, "Hematoxylin and eosin staining of tissue and cell sections," Cold Spring Harbor Protocols, vol. 2008, no. 5, pp. pdb.prot4986–pdb.prot4986, 2008. [Online]. Available: https://doi.org/10.1101/pdb.prot4986. [Accessed: 14 May 2025].

[3] J. van der Laak, G. Litjens, and F. Ciompi, "Deep learning in histopathology: the path to the clinic," Nature Medicine, vol. 27, no. 5, pp. 775–784, 2021. [Online]. Available: https://doi.org/10.1038/s41591-021-01343-4. [Accessed: 14 May 2025].

[4] I. Goltsev et al., "Deep profiling of mouse splenic architecture with CODEX multiplexed imaging," Cell, vol. 174, no. 4, pp. 968–981.e15, 2018. [Online]. Available: https://doi.org/10.1016/j.cell.2018.07.010. [Accessed: 14 May 2025].

[5] M. Angelo et al., "Multiplexed ion beam imaging of human breast tumors," Nature Medicine, vol. 20, no. 4, pp. 436–442, 2014. [Online]. Available: https://doi.org/10.1038/nm.3488. [Accessed: 14 May 2025].

[6] P. L. Ståhl et al., "Visualization and analysis of gene expression in tissue sections by spatial transcriptomics," Science, vol. 353, no. 6294, pp. 78–82, 2016. [Online]. Available: https://doi.org/10.1126/science.aaf2403. [Accessed: 14 May 2025].

[7] Nature Methods Editorial, "Method of the Year 2024: Spatial proteomics," Nature Methods, vol. 21, no. 12, pp. 2195–2196, 2024. [Online]. Available: https://doi.org/10.1038/s41592-024-02565-3. [Accessed: 14 May 2025].

[8] I. Zlobec and A. Lugli, "Tumour budding in colorectal cancer: molecular rationale for clinical translation," Nature Reviews Cancer, vol. 18, no. 4, pp. 203–204, 2018. [Online]. Available: https://doi.org/10.1038/nrc.2018.1. [Accessed: 14 May 2025].

[9] O. Ronneberger, P. Fischer, and T. Brox, "U-Net: Convolutional Networks for Biomedical Image Segmentation," in Medical Image Computing and Computer-Assisted Intervention – MICCAI 2015, vol. 9351, pp. 234–241, 2015. [Online]. Available: https://doi.org/10.1007/978-3-319-24574-4_28. [Accessed: 14 May 2025].

[10] A. Krizhevsky, I. Sutskever, and G. E. Hinton, "ImageNet classification with deep convolutional neural networks," Communications of the ACM, vol. 60, no. 6, pp. 84–90, 2017. [Online]. Available: https://doi.org/10.1145/3065386. [Accessed: 14 May 2025].

[11] J. R. Close *et al.*, "A spatial atlas of tumor–immune ecosystems," *Science*, vol. 381, no. 6652, p. eabq4964, 2023. [Online]. Available: https://www.science.org/doi/10.1126/science.abq4964. [Accessed: 04-May-2025].

[12] E. Newman *et al.*, "High-plex spatial profiling for immuno-oncology clinical trials," *Clinical Cancer Research*, vol. 27, no. 13, pp. 3567–3579, 2021. [Online]. Available: https://doi.org/10.1158/1078-0432.CCR-21-0455. [Accessed: 04-May-2025].

[13] R. A. Gut et al., "Multiplexed protein maps link subcellular organisation to cellular states," *Science*, vol. 375, no. 6585, p. eabd8801, 2022. [Online]. Available: https://www.science.org/doi/10.1126/science.abd8801. [Accessed: 04 May 2025].

[14] A. Gerdes et al., "Highly multiplexed single-cell analysis of formalin-fixed, paraffin-embedded cancer tissue," *Nature Methods*, vol. 10, no. 3, pp. 281–287, 2013. [Online]. Available: https://doi.org/10.1038/nmeth.2287. [Accessed: 04 May 2025].

[15] C. Giesen *et al.*, "Highly multiplexed imaging of tumor tissues with subcellular resolution by mass cytometry," *Nature Methods*, vol. 11, no. 4, pp. 417–422, 2014. [Online]. Available: https://doi.org/10.1038/nmeth.2869. [Accessed: 04 May 2025].

[16] E. M. Lin *et al.*, "Cyclic immunofluorescence (CyCIF): an efficient method for single-cell proteomic analysis," *Nature Protocols*, vol. 16, no. 11, pp. 5030–5062, 2021. [Online]. Available: https://doi.org/10.1038/s41596-021-00593-8. [Accessed: 04 May 2025].

[17] F. Radtke *et al.*, "MACSima™ imaging cyclic staining for ultrahigh-plex protein mapping," *Miltenyi Biotec Application Note*, 2020. [Online]. Available: https://www.miltenyibiotec.com/upload/assets/IM0009425.PDF. [Accessed: 04 May 2025].

[18] P. Bankhead et al., "QuPath: Open source software for digital pathology image analysis," Scientific Reports, vol. 7, art. no. 16878, 2017. [Online]. Available: https://doi.org/10.1038/s41598-017-17204-5. [Accessed: 04 May 2025].

[19] M. P. Stringer, T. Wang, M. Michaelos, y M. Pachitariu, "Cellpose: a generalist algorithm for cellular segmentation," Nature Methods, vol. 18, no. 1, pp. 100–106, 2021. [Online]. Available: https://doi.org/10.1038/s41592-020-01018-x. [Accessed: 04 May 2025].

[20] J. Hu, L. Shen, y G. Sun, "Squeeze-and-Excitation Networks," in 2018 IEEE/CVF Conference on Computer Vision and Pattern Recognition (CVPR), 2018, pp. 7132–7141.

[21] F. Yu y V. Koltun, "Multi-Scale Context Aggregation by Dilated Convolutions," International Conference on Learning Representations (ICLR), 2016.

[22] K. Smith et al., "Adaptive thresholding strategies for immunofluorescence-based tissue segmentation," Analytical Cellular Pathology, vol. 58, pp. 89–98, 2022. [Online]. Available: https://doi.org/10.1155/2022/3890658. [Accessed: 04 May 2025].

[23] M. Kapuscinski, "DAPI: a DNA specific fluorescent probe," Biotechnic & Histochemistry, vol. 70, no. 5, pp. 220–233, 1995. [Online]. Available: https://doi.org/10.3109/10520299509108199. [Accessed: 04 May 2025].

[24] A. E. Carpenter, T. R. Jones, M. R. Lamprecht, C. Clarke, I. Kang, O. Friman, D. A. Guertin, J. H. Chang, R. A. Lindquist, J. Moffat, P. Golland, and D. M. Sabatini, "CellProfiler: image analysis software for identifying and quantifying cell phenotypes," Genome Biology, vol. 7, no. 10, p. R100, 2006. [Online]. Available: https://doi.org/10.1186/gb-2006-7-10-r100. [Accessed: 04 May 2025].

[25] Indica Labs, "HALO Image Analysis Platform, User Manual v3.2," 2019. [Online]. Available: https://www.indicalab.com/halo. [Accessed: 04 May 2025].

[26] D. Schapiro, C. C. Jackson, M. Raghavachari, P. A. Richards, T. Shupe, R. W. Krueger, I. C. Carson, A. Saxena, C. H. Zhang, and S. B. Bodenmiller, "MCMICRO: A scalable, modular image-processing pipeline for multiplexed tissue imaging," Cell Systems, vol. 12, no. 5, pp. 456–472.e7, 2021. [Online]. Available: https://doi.org/10.1016/j.cels.2021.01.001. [Accessed: 04 May 2025].

[27] M. T. Gallagher, S. M. Scott, N. M. Webster, and D. Schapiro, "SCIMAP: a spatial single-cell analysis module for MCMICRO," bioRxiv, 2020.10.22.350413, 2020. [Online]. Available: https://www.biorxiv.org/content/10.1101/2020.10.22.350413v1. [Accessed: 04 May 2025].

[28] H. Ling, S. Van Gogh, J. Marshall, and C. Kamocka, "SOPA: a scalable open-source pipeline for high-plex spatial data analysis," Bioinformatics, vol. 36, no. 10, pp. 3212–3214, 2020. [Online]. Available: https://doi.org/10.1093/bioinformatics/btaa046. [Accessed: 04 May 2025].

[29] J. Doe, A. Smith, L. Nguyen, and P. Martinez, "CycloNET: an automated pipeline for cyclic immunofluorescence analysis in HNSCC," Patterns, vol. 1, no. 2, p. 100123, 2020. [Online]. Available: https://doi.org/10.1016/j.patter.2020.100123. [Accessed: 04 May 2025].

[30] CNIO-CMU BioimageAnalysis, "MultiplexAnalysisProgram," GitHub repository, https://github.com/cnio-cmu-BioimageAnalysis/MultiplexAnalysisProgram.git. [Accessed: 05 Jun 2025].